Bioactive Materials 19 (2023) 626–641

Contents lists available at ScienceDirect

Bioactive Materials

journal homepage: www.keaipublishing.com/en/journals/bioactive-materials

Apoptotic extracellular vesicles are metabolized regulators nurturing the skin and hair

Lan Ma [a,b], Chider Chen [b], Dawei Liu [b,c], Zhiqing Huang [a], Jiaqi Li [a], Haixiang Liu [d], Ryan Tsz Kin Kwok [d], Benzhong Tang [e], Bingdong Sui [a,b], Xiao Zhang [a,b], Jianxia Tang [a,b], Xueli Mao [a], Weiying Huang [a], Songtao Shi [a,b,f,**], Xiaoxing Kou [a,b,f,*]

[a] Hospital of Stomatology, Guanghua School of Stomatology, Sun Yat-sen University, South China Center of Craniofacial Stem Cell Research, Guangdong Provincial Key Laboratory of Stomatology, 510055, Guangzhou, China
[b] Department of Anatomy and Cell Biology, University of Pennsylvania, School of Dental Medicine, Philadelphia, PA, 19104, USA
[c] Department of Orthodontics, Peking University School & Hospital of Stomatology, #22 Zhongguancun South Avenue, Beijing, 100081, China
[d] Department of Chemical and Biological Engineering, Department of Chemistry, The Hong Kong Branch of Chinese National Engineering Research Center for Tissue Restoration and Reconstruction and Institute for Advanced Study, The Hong Kong University of Science and Technology, Clear Water Bay, Kowloon, Hong Kong, China
[e] Shenzhen Institute of Aggregate Science and Technology, School of Science and Engineering, The Chinese University of Hong Kong, Shenzhen, 2001 Longxiang Boulevard, Longgang District, Shenzhen City, Guangdong, 518172, China
[f] Key Laboratory of Stem Cells and Tissue Engineering (Sun Yat-Sen University), Ministry of Education, Guangzhou, Guangdong, 510055, China

ARTICLE INFO

Keywords:
Apoptosis
Extracellular vesicle
Metabolized regulator
Integumentary system
Mesenchymal stem cells

ABSTRACT

Over 300 billion of cells die every day in the human body, producing a large number of endogenous apoptotic extracellular vesicles (apoEVs). Also, allogenic stem cell transplantation, a commonly used therapeutic approach in current clinical practice, generates exogenous apoEVs. It is well known that phagocytic cells engulf and digest apoEVs to maintain the body's homeostasis. In this study, we show that a fraction of exogenous apoEVs is metabolized in the integumentary skin and hair follicles. Mechanistically, apoEVs activate the Wnt/β-catenin pathway to facilitate their metabolism in a wave-like pattern. The migration of apoEVs is enhanced by treadmill exercise and inhibited by tail suspension, which is associated with the mechanical force-regulated expression of DKK1 in circulation. Furthermore, we show that exogenous apoEVs promote wound healing and hair growth *via* activation of Wnt/β-catenin pathway in skin and hair follicle mesenchymal stem cells. This study reveals a previously unrecognized metabolic pathway of apoEVs and opens a new avenue for exploring apoEV-based therapy for skin and hair disorders.

1. Introduction

Apoptosis represents a form of programmed cell death that contributes to the elimination of excess and damaged cells from an organism without disrupting tissue and organ integrity [1,2]. It is a necessary process to ensure organ growth and development as well as maintenance of adult organ homeostasis [3]. Apoptotic cells undergo a series of biological events, including blebbing, cell shrinkage, nuclear fragmentation, chromatin condensation and chromosomal DNA fragmentation to form apoptotic extracellular vesicles (apoEVs), which contain cellular components including microRNAs, mRNAs, DNAs, proteins, and lipids [4–6]. Eventually, apoEVs are cleared by different phagocytes, such as professional phagocytes, non-professional phagocytes and specialized phagocytes, after presenting "Find-Me" signals that promote the engulfment process [7–9]. In addition, apoEVs play an important role in intercellular communication, immune modulation, procoagulant activity, and maintenance of tissue homeostasis [9–12]. It is believed that around 50–70 billion cells undergo apoptosis in an adult human each

Peer review under responsibility of KeAi Communications Co., Ltd.

* Corresponding author. Hospital of Stomatology, Guanghua School of Stomatology, Sun Yat-sen University, South China Center of Craniofacial Stem Cell Research, Guangdong Provincial Key Laboratory of Stomatology, 510055, Guangzhou, China.

** Corresponding author. Hospital of Stomatology, Guanghua School of Stomatology, Sun Yat-sen University, South China Center of Craniofacial Stem Cell Research, Guangdong Provincial Key Laboratory of Stomatology, 510055, Guangzhou, China.

E-mail addresses: songtaos@upenn.edu (S. Shi), kouxiaoxing@mail.sysu.edu.cn (X. Kou).

https://doi.org/10.1016/j.bioactmat.2022.04.022
Received 17 October 2021; Received in revised form 20 March 2022; Accepted 20 April 2022

day, generating a large number of endogenous apoEVs [3,13,14]. The metabolic pathway of these apoEVs may have a significant impact on the biological activities of multiple organ systems and the development of numerous diseases.

Mesenchymal stem cells (MSCs) have been used in the clinics to treat a variety of diseases, such as systemic lupus erythematosus (SLE), graft versus host disease (GvHD), rheumatoid arthritis and multiple sclerosis, as well as to mediate tissue regeneration [15–19]. MSC transplantation can generate exogenous apoEVs capable of regulating endogenous MSC function and maintaining bone homeostasis [11]. However, the detailed functional role of apoEVs is largely unknown. In this study, we show that exogenous apoEVs are metabolized in the integumentary system as well as maintaining skin and hair homeostasis.

2. Results

2.1. Identification of MSC-derived apoEVs

We used staurosporine (STS) to induce apoptosis of culture-expanded murine MSCs and then isolated apoEVs using a sequential centrifuge system (Fig. 1A). After 16 h of STS induction, MSCs showed significant morphological alteration and apoptotic responses as assessed by TUNEL assay and flow cytometry analysis with annexin V and 7AAD staining (Fig. 1B–E). We used transmission electron microscopy (TEM), nanoparticle track analysis (NTA), and nanoflow cytometric analysis to confirm the morphology and size of newly isolated apoEVs (Fig. 1F–H). Small extracellular vesicles (sEVs) isolated from MSCs were used as a control (Figs. S1A–C). To further confirm the purity of apoptotic MSC-generated apoEVs, we used Western blotting analysis to show that apoEVs expressed common extracellular vesicles (EVs) markers CD9 and TSG101, but failed to express exosomes-specific marker syntenin-1. ApoEVs expressed high levels of apoptosis-associated markers such as cleaved caspase-3 and calreticulin [20] (Fig. 1I). In addition, we found that cleaved lamin B1, a caspase-3 substrate of the inner nuclear membrane [21], was detected in apoEVs, but not in sEVs. Next, we used nanoflow cytometric and super-resolution structured illumination microscopy (SIM) analysis to confirm that apoEVs expressed a higher level of phosphatidylserine (PtdSer, shown by Annexin V binding, 80.2%), calreticulin (41.2%) and lamin B1 (28.4%) (Fig. 1J and K). In contrast, sEVs only expressed a lower level of PtdSer (18.5%) as well as limited levels of calreticulin (3.2%) and lamin B1 (4.6%) (Figs. S1D and E).

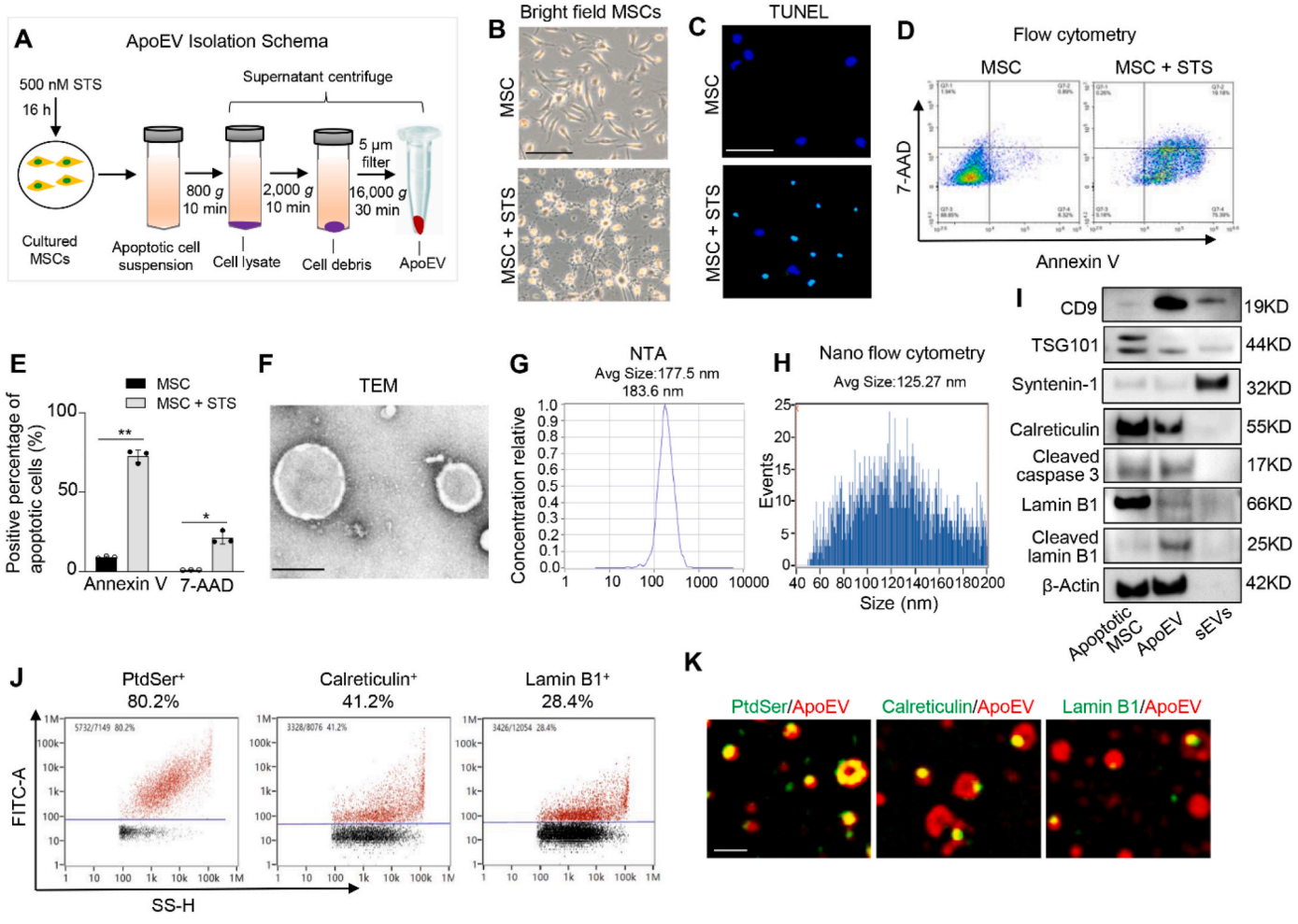

Fig. 1. Isolation and characteristics of apoEVs. **(A)** ApoEV isolation schema. Murine MSCs are induced by 500 nM STS for 16 h and then apoptotic cell suspensions are isolated using a sequential centrifuge system to get fresh apoEVs. **(B)** MSCs show morphological change after 16 h of STS induction observed under the microscopy. **(C)** TUNEL assay show the apoptotic cell after STS induction as indicated by TUNEL positive cell (green). **(D, E)** Flow cytometry analysis of MSCs apoptosis after STS treatment. n = 3. *P < 0.05, **P < 0.01, student's t-test. Data shown as mean ± SD. **(F)** TEM assay confirm the morphology of apoEVs. **(G, H)** NTA assay and nanoflow cytometry analysis show the size distribution of apoEVs. **(I)** Western blotting shows the expression levels of CD9, TSG101, syntenin-1, calreticulin, cleaved caspase 3, lamin B1, cleaved lamin B1 and β-Actin in apoptotic MSCs, apoEVs and small EVs (sEVs). **(J, K)** Nanoflow cytometry and immunofluorescent staining show apoEVs express apoptotic body-specific surface markers Ptdser (shown by Annexin V staining), calreticulin and lamin B1. Scale bar (B), 100 μm; Scale bar (C), 50 μm; Scale bar (F), 200 nm; Scale bar (K), 1 μm.

2.2. ApoEVs migrated to the integumentary system

To assess the *in vivo* distribution of apoEVs, 4×10^6 DIR-labeled apoEVs were intravenously infused into immunocompromised mice. Intravital imaging showed the distribution of apoEVs throughout the body at 1, 3 and 7 days after the infusion (Fig. S2A). The peak of apoEV appearance occurred at 3 days and significantly decreased at 7 days post-infusion (Fig. S2A). The majority of infused apoEVs accumulated in the liver, skin, spleen and lung (Fig. S2B), which was further confirmed by immunofluorescent analysis (Fig. S2C).

The integumentary system, mainly comprises the skin and hair, plays multiple roles in maintaining the body's homeostasis, including an excretory function [22]. Our results indicate that exogenous apoEVs can be partly eliminated through the integumentary system. The outer stratum corneum of the skin is shed at a rate of 28–85 mg per hour throughout a person's life [23], and it is estimated that a normal person loses 50–100 hairs per day [24]. Indeed, we detected systemically infused apoEVs in the stratum corneum layer (Fig. 2A). Therefore, we hypothesized that exogenous infused apoEVs could be partly eliminated from the integumentary system *via* skin and hair shedding.

To test our hypothesis, we examined the destinations of intravenously infused apoEVs. Immunofluorescent staining showed that systemically infused apoEVs, labeled with PKH26 (PKH26-ApoEV) or GFP (GFP-ApoEV), migrated to the skin and pre-exfoliated stratum corneum (Fig. 2A and B) when compared to the control group (Fig. S3A). Western blotting results confirmed that GFP-labeled apoEVs were located in the skin at 7 days post-infusion (Fig. 2B). Moreover, when DIR-labeled apoEVs (DIR-ApoEV) were injected into BALB/c-nu/nu mice *via* the

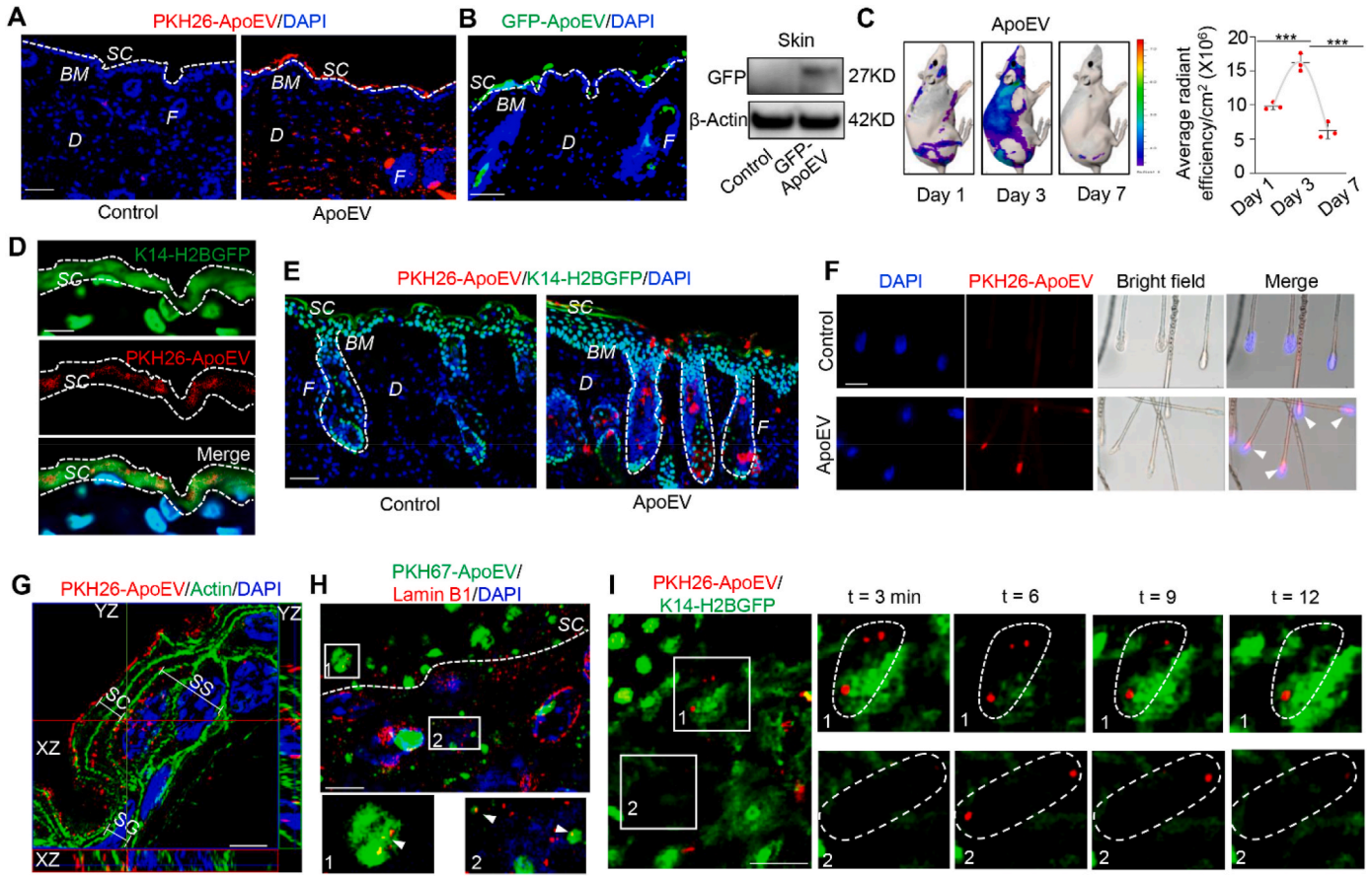

Fig. 2. ApoEVs are metabolized from the skin and hair follicles. **(A)** Immunofluorescent staining shows the distribution of apoEVs in the skin. PKH26-labeled apoEVs (4×10^6) were injected into C57BL/6 mice *via* the tail vein. White dotted line represents the dividing layer between stratum corneum (*SC*) and the other layers of epidermis. **(B)** Immunofluorescent image shows GFP-ApoEV migrated to the stratum corneum after systemic injection. Western blotting shows GFP signal was detected in the skin tissue after GFP-ApoEV injection. **(C)** Analog images and quantification graph show time-dependent apoEVs fluorescence intensity changes in the skin at 1, 3 and 7 days post-injection. DIR-labeled apoEVs were systemically injected into BALB/c-nu/nu mice. After sacrificing mice at 1, 3, 7 days post-injection, *ex vivo* skin images were collected in 745 nm channel with laser excitation at 800–820 nm using an IVIS spectrum imaging system (PerKin Elmer). n = 3. ***$P < 0.001$, one-way ANOVA test. Data shown as mean ± SD. **(D)** Immunofluorescent images show PKH26-ApoEV (red) at the position around stratum corneum (green). PKH26-labeled apoEVs (4×10^6) were injected into K14–H2BGFP mice. White dotted line represents the border of stratum corneum. **(E)** Immunofluorescent staining showed the distribution of apoEVs from dermal papillae to the stratum corneum through the hair follicle post-injection. PKH26-labeled apoEVs (4×10^6) were injected into K14–H2BGFP mice. White dotted line represents the outer shape of hair follicles. **(F)** ApoEVs were observed in the hair bulbs of extracted hair. PKH26-labeled apoEVs (4×10^6) were injected into C57BL/6 mice. Arrow heads indicated apoEVs in the hair bulbs. **(G)** Super-resolution SIM microscopy analysis shows the intracellular and extracellular location of apoEVs in different epidermal layers. PKH26-labeled apoEVs (red) were detected inside the cells containing nucleus (SS), the cells losing nucleus (SG), and outside the cells without nucleus (SC) in different epidermal layers. The skin sections were stained with actin (green) to show the outline of epidermal cells. The white bars indicate the different layers of epidermis. **(H)** Immunofluorescent staining shows colocalization of apoEVs (green) with lamin B1 (red) in the skin at day 3. The lower panels magnify the boxed areas in the top panel. **(I)** Two-photon laser-scanning microscopy (TPLSM) shows the dynamic shedding of PKH26-labeled apoEVs in the epidermis of live K14–H2BGFP mice. The left panel shows images of two different positions (1 and 2). The right panels are higher magnification sequential images of the boxed regions. The dotted line areas indicate the dynamic change of apoEVs at different time points. SC, stratum corneum; SG, stratum granulosum; SS, stratum spinosum; BM, basement membrane; F, hair follicle; D, dermis. Scale bars (A, B, E, F), 50 μm; Scale bars (D, I), 20 μm; Scale bars (G, H), 5 μm.

tail vein, we found that MSC-derived apoEVs were distributed in the skin at 1, 3 and 7 days after injection (Fig. 2C). Exogenously infused MSCs showed a similar distribution pattern as the apoEV-infused group in the skin and hair follicles (Figs. S3B–D). Interestingly, fluorescent image intensity in the skin reached a peak at day 3 and significantly reduced at day 7 after apoEV infusion, indicating that both infused MSCs and exogenous apoEVs are excreted through the skin (Fig. 2C and Fig. S3D). To avoid the potential that lipophilic membrane labeling disturbs membrane integrity [25], we labeled apoEVs with DCPy, an AIEgen (Aggregation induced emission luminogen) based photosensitizer targeting at mitochondria capable of inducing apoptosis by generating reactive oxygen species (ROS) upon light irradiation [26,27]. In this way, apoEVs were generated and labeled simultaneously. We confirmed that AIEgen labeled apoEVs (AIEgen-ApoEV) existed in the stratum corneum and hair follicles (Fig. S3E). Using the K14–H2BGFP mice [28], we confirmed that apoEVs were located in the stratum corneum layer (Figs. 2D and S3F). To further confirm that apoEVs are shed during skin and hair turnover, we used immunofluorescent image analysis to show that apoEVs migrated to the epidermis, as indicated by co-staining with keratin 14 (K14), a marker of the epidermis and outer root sheath (Fig. S3F). We also observed the existence of infused apoEVs from the hair bulb to the stratum corneum (Fig. 2E). After 4×10^6 PKH26-labeled apoEVs were systemically injected into C57BL/6 mice, apoEVs were detected in the hair bulbs of extracted hairs (Fig. 2F). These data imply that apoEVs are metabolized upon hair shedding.

In order to reveal how apoEVs are eliminated from the skin surface, we used super-resolution SIM microscopy to display the detailed location of infused apoEVs in the epidermis. In the stratum spinosum of the epidermis, the systemic-infused PKH26-ApoEV, GFP-ApoEV, and AIEgen- ApoEV were located mainly inside the cells. Three-dimensional reconstruction of Z-stack SIM microscopy images confirmed that the labeled-apoEV signals were localized between actin and nuclei (Figs. 2G and S3G). Moreover, labeled-apoEVs are located both inside and outside the cells in the non-nucleated stratum corneum, indicating that apoEVs may be metabolized by shedding stratum corneum cells.

Co-localization of PKH67 labeled apoEVs and apoEV marker lamin B1 further identified the presence of apoEVs in the skin (Fig. 2H). Next, we used a parabiosis mouse model, which has been utilized to study circulatory factors transferring from one animal to another [11,29], to assess whether natural apoEVs could circulate from GFP mice to parabiotically connected wild-type mice. Immunofluorescent staining showed that GFP signals were detected in the stratum corneum and dermis of the wild-type mice with co-expression of apoEV marker lamin B1 (Fig. S3H), indicating that circulating apoEVs could be metabolized and cleared from the integumentary system. To investigate the movement of apoEVs during their excretion within living mice, we used two-photon laser-scanning microscopy (TPLSM) to record the dynamic movement of PKH26-labeled apoEVs in the epidermis of K14–H2BGFP mice at 3 days post-infusion [30,31]. We visualized apoEVs in the epidermis at an interval of 3 min for 0.5 h (Fig. 2I and Movie S1). It confirmed that apoEV elimination from the skin was a continuous process, consistent with the rapid turnover rate of skin. Our results indicate that transplanted or natural apoptotic cell-derived apoEVs are partly metabolized through the integumentary skin and hair follicle.

2.3. Wnt/β-catenin pathway is required for apoEVs migration

Next, we examined the mechanism that may control apoEV migration. Wnt/β-catenin signaling pathway plays a critical role in skin and hair development [32,33]. Our previous study showed that apoEVs upregulated Wnt/β-catenin signaling in recipient MSCs [11]. Here, we revealed that infused apoEVs could activate the Wnt/β-catenin pathway in the skin, as indicated by Western blotting and immunofluorescent staining (Fig. 3A and B). We also used 5-ethynyl-2′-deoxyuridine (EdU) staining to show that infused apoEVs accelerated the turnover rate of the skin in K14–H2BGFP mice, especially around the basal layer of the interfollicular epidermis (IFE), in which epidermal stem cells control epidermal turnover (Fig. 3C) [33].

To further explore the functional role of Wnt/β-catenin pathway in regulating apoEV migration, we used Wnt signaling pathway activator lithium chloride (LiCl) [34] and inhibitor XAV939 [35] to regulate the expression of active-β-catenin (Fig. 3D). Immunofluorescent images and Western blotting results showed that LiCl treatment increased the number of GFP-positive apoEVs migrating to the stratum corneum at 7 days post-infusion (Fig. 3E and F). In contrast, XAV939 treatment reduced the number of GFP-positive apoEVs migrating to the stratum corneum at 7 days post-infusion (Fig. 3E and F), suggesting that Wnt/β-catenin pathway regulates the secretion of apoEVs. To verify the direct correlation between Wnt/β-catenin signaling and apoEVs, we showed that apoEVs directly upregulated the expression level of active-β-catenin in the skin tissue, which was blocked by XAV939 treatment along with the reduced secretion of apoEVs in the skin (Fig. 3G). Moreover, immunofluorescent staining showed that apoEV infusion enhanced the turnover rate of the skin in K14–H2BGFP mice, which was also blocked by XAV939 treatment along with reduced number of apoEVs in the skin (Fig. 3H). To further confirm the functional role of apoEVs in the skin, we used Western blotting to show that apoEVs, but not control vesicles with phosphatidylserine (PS), activated the Wnt/β-catenin pathway in the skin (Fig. 3I). Immunofluorescent staining showed that artificial liposome vesicles (200 nm) containing 2% Cy3 and PS failed to migrate into the epidermis (Fig. 3J).

2.4. Mechanical force regulates the metabolism of apoEVs in the skin

It is well-known that Wnt/β-catenin pathway regulates skin stem cells proliferation and turnover. We found that apoEVs can activate Wnt/β-catenin pathway from day 1 to day 7 of the post-infusion, which may be an impetus to accelerate apoEV migration in the skin. ApoEV-induced up-regulation of Wnt/β-catenin in the skin returned to normal after 10 days post-infusion. In addition, EdU staining showed that the proliferation rate of skin cells increased at day 3 and decreased around day 7 of post-apoEVs injection (Figs. 4A, B, and S4).

Interestingly, the excreted apoEVs showed a multi-layer wave-like pattern from the basal to the surface of the epidermis (Fig. 4C). Since mechanical forces play diverse roles in modulating biological processes [36–39], we explore the potential correlation between mechanical forces and the pattern of apoEV migration. We used treadmill exercise to increase mechanical force and tail suspension to reduce it (Fig. 5A). Immunofluorescent images and Western blotting results showed that treadmill exercise increased the number of GFP-positive apoEVs migrating to the stratum corneum at 7 days post-infusion. In contrast, tail suspension decreased the number of GFP-positive apoEVs migrating to the stratum corneum at 7 days post-infusion (Fig. 5B and C), implying that mechanical force regulates the migration of apoEVs. After infusion of 4×10^6 PKH67-labeled apoEVs, we found that $PKH67^+$/Annexin V^+/$CD62P^-$ apoEVs in the circulation were reduced in the treadmill exercise group but increased in the tail suspension group compared to the control group (Fig. 5D and E). Moreover, we revealed that treadmill exercise increased skin elimination of DIR-labeled apoEVs after 0.5 days post apoEVs infusion whereas tail suspension reduced skin secretion of DIR-labeled apoEVs compared to the control group at 3 days post apoEV infusion (Fig. 5F and G). Consistent with previous reports that mechanical force can regulate Wnt/β-catenin pathway [40,41], we found that treadmill exercise reduced the level of Dickkopf-1 (DKK-1), an endogenous inhibitor of Wnt signaling, but tail suspension enhanced the level of DKK-1 in the circulation (Fig. 5H). Next, we used immunofluorescent staining to show that treadmill exercise enhanced apoEV-induced expression of active-β-catenin in skin, but tail suspension reduced it. On the contrary, the expression level of DKK1 was inhibited in the treadmill running group but increased in the tail suspension group (Fig. 5I). Our results indicate that mechanical force regulates the metabolism of apoEVs through Wnt/β-catenin pathway.

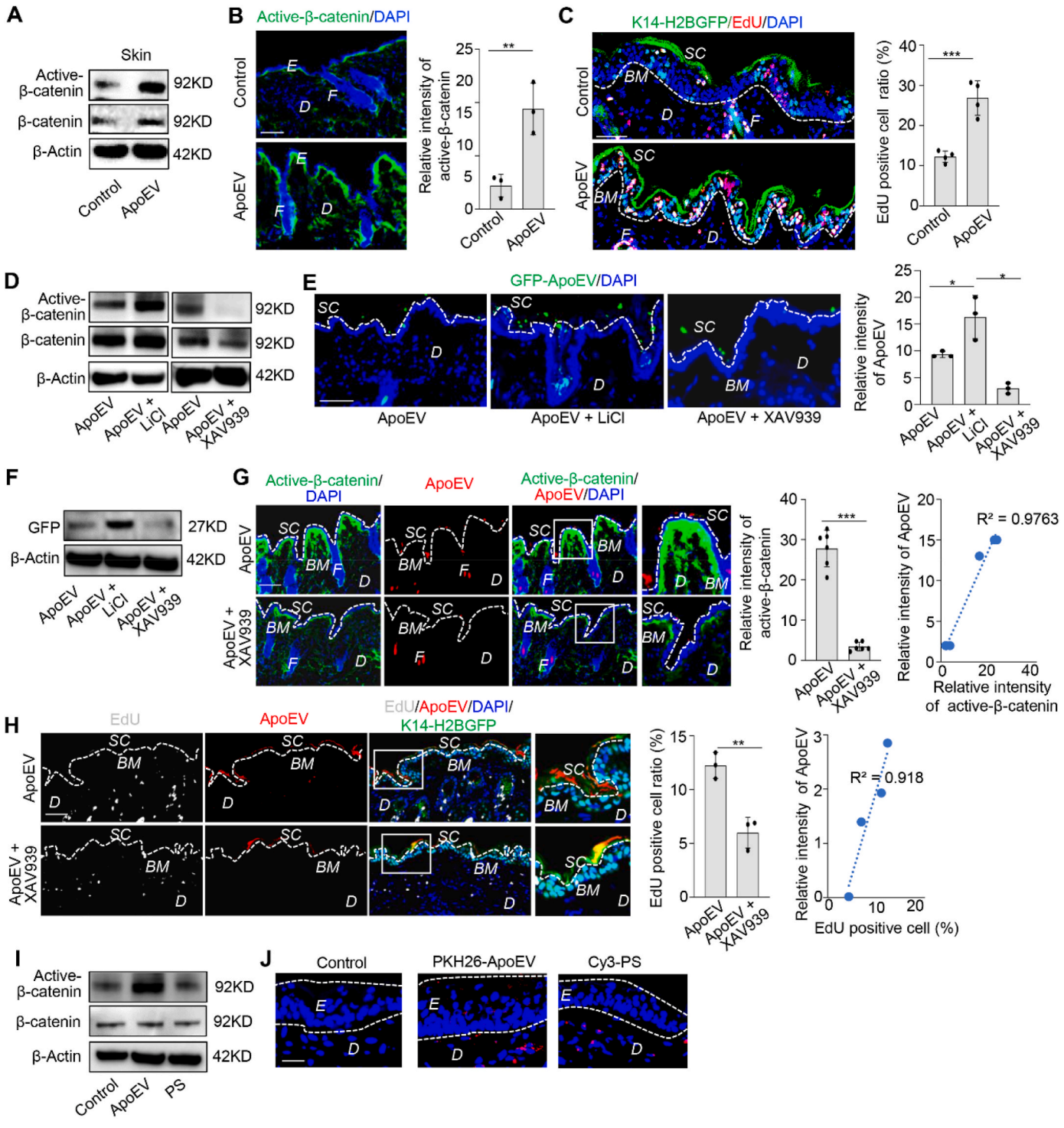

(caption on next page)

Fig. 3. Wnt/β-catenin pathway is required for apoEVs migration. **(A)** Western blotting shows the systemically infused apoEVs increased the expression level of active β-catenin in the skin. **(B)** Immunofluorescent images show apoEVs upregulated Wnt/β-catenin signaling (green) in the skin of C57BL/6 mice after systemically infusion. The relative intensity of activated β-catenin was calculated. n = 3. **P < 0.01, Student's *t*-test. Data shown as mean ± SD. **(C)** EdU staining shows that systemically infused apoEVs accelerated the turnover rate of the skin in K14–H2BGFP mice, especially in the basal layer. Dotted lines demarcate dermal-epidermal junction. n = 4. ***P < 0.001, Student's *t*-test. Data shown as mean ± SD. **(D)** Western blotting analysis shows that LiCl treatment upregulated the expression level of active β-catenin in apoEV-treated mice. In contrast, XAV939 treatment reduced the level of active β-catenin expression in apoEV-treated mice. **(E)** Immunofluorescent images show the number of GFP-ApoEV migrating to the epidermis was increased in LiCl treatment group and reduced in XAV939 treatment group at 7 days post-injection. White dotted line represents the dividing layer between stratum corneum and the other layers of epidermis. n = 3. *P < 0.05, one-way ANOVA test. Data shown as mean ± SD. **(F)** Western blotting confirmed the level of GFP in the skin tissue was increased in LiCl treatment group and reduced in XAV939 treatment group. **(G)** Immunofluorescent images show XAV939 treatment reduced the expression level of Wnt/β-catenin and inhibited apoEVs secretion from the skin. Panel includes higher magnification of the boxed region to show localization of apoEVs. White dotted line represents the dividing layer between stratum corneum and the other layers of epidermis. The correlation between apoEVs and active-β-catenin was calculated. n = 6. ***P < 0.001, Student's *t*-test. Data shown as mean ± SD. **(H)** Immunofluorescent images show XAV939 treatment reduced the turnover rate and apoEV (red) elimination from the skin. Panel includes higher magnification of the boxed region to show the intensity of apoEVs at the epidermis. The correlation between apoEVs elimination and turnover rate was calculated. n = 3. **P < 0.01, Student's *t*-test. Data shown as mean ± SD. **(I)** Western blotting shows that treatment with apoEVs, but not synthetic lipid vesicles containing PS, activates Wnt/β-catenin signaling in the skin. **(J)** Immunofluorescent images show the location of PKH26-ApoEV and Cy3-PS in the skin. White dotted lines indicated the boundary of epidermis. SC, stratum corneum; BM, basement membrane; F, hair follicle; D, dermis; E, epidermis. Scale bars (B, C, E, G, H), 50 μm; Scale bar (J), 25 μm.

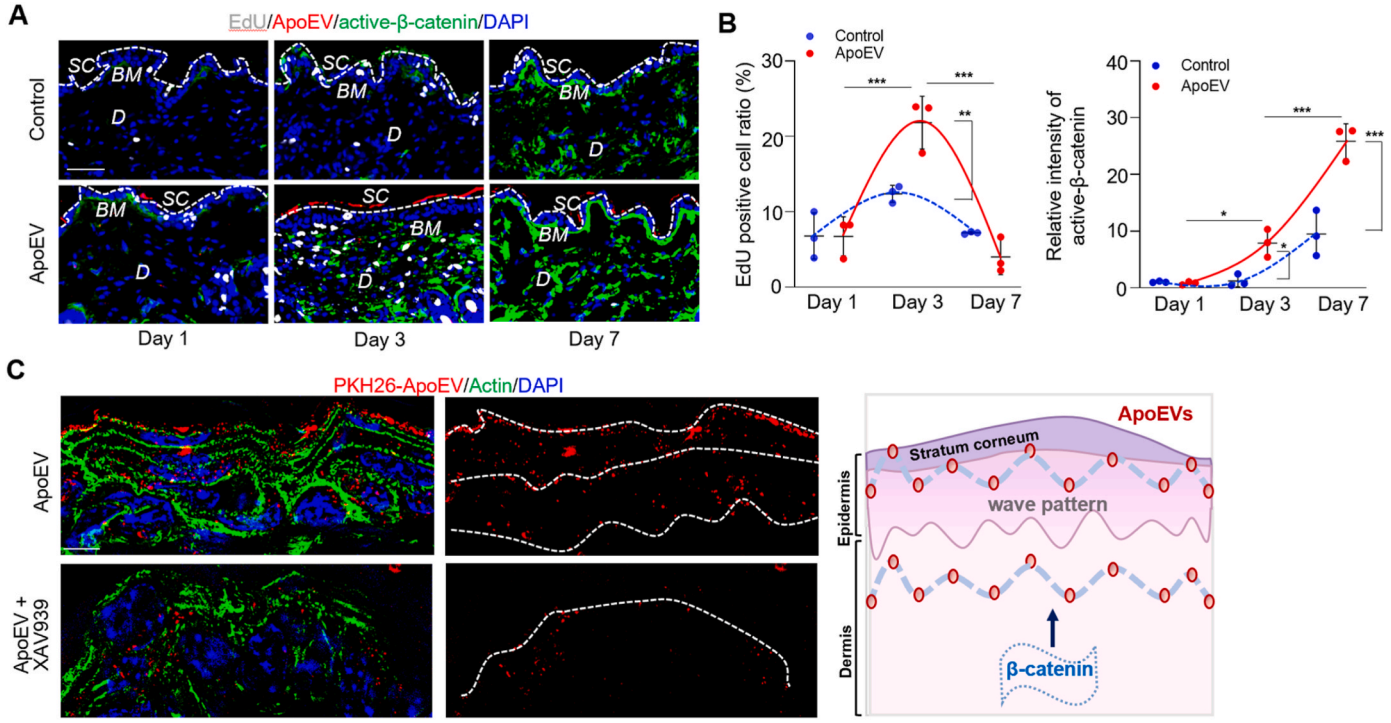

Fig. 4. ApoEV metabolism shows a wave-like movement pattern. **(A)** Immunofluorescent staining shows the proliferate rate change in the skin on days 1, 3 and 7 with or without apoEVs injection, indicated by EdU staining. The activity of Wnt/β-catenin pathway and the elimination of apoEVs are observed at the same time. White dotted line represents the dividing layer between stratum corneum and the other layers of epidermis. **(B)** Quantification graph shows the change of EdU positive cell ratio and fluorescent intensity of Wnt/β-catenin in the skin from day 1 to day 7 after apoEVs injection. n = 3. *P < 0.05, **P < 0.01, ***P < 0.001, one-way ANOVA test. Data shown as mean ± SD. **(C)** Immunofluorescent staining shows the wave pattern when apoEVs are cleared in the skin, but XAV939 treatment interferes with the pattern, as indicated by the schematic graph. The white dotted lines simulate the pattern of apoEVs. SC, stratum corneum; BM, basement membrane; D, dermis. Scale bar (A), 50 μm; Scale bars (C), 5 μm.

2.5. *ApoEVs rescue impaired skin and hair follicle MSCs*

MRL/*lpr* mice with Fas mutation are considered as an apoptosis-deficient model [11,42]. Our previous study showed that bone marrow MSCs from MRL/*lpr* mice are significantly impaired, which could be rescued by phagocytosis of exogenous apoEVs [11]. Therefore, we hypothesized that skin MSCs (SMSCs) and hair follicle MSCs (HF-MSCs) in MRL/*lpr* mice might be impaired due to lack of secreted apoEVs, and infusion of exogenous apoEVs could rescue this impairment. SMSCs and HF-MSCs were isolated and characterized by flow cytometric analysis (Fig. S5). To test our hypothesis, apoEVs isolated from GFP-MSCs were subcutaneously injected into MRL/*lpr* mice. Immunofluorescent image analysis showed that GFP-apoEVs were engulfed by CD105-positive SMSCs, which was further confirmed by Western blotting analysis (Fig. 6A and B). Moreover, immunofluorescent staining of SMSC smears showed that SMSCs could endocytose apoEVs (Fig. 6C). ApoEV-infusion activated Wnt/β-catenin pathway and decreased DKK1 expression in SMSCs and HF-MSCs, as assessed by Western blotting (Fig. 6D). When 4×10^6 apoEVs were subcutaneously infused, impaired SMSCs and HF-MSCs from MRL/*lpr* mice were rescued, as indicated by increased EdU labeling and population doubling rates, enhanced mineralized nodule formation, elevated expression of Runx2 and ALP, improved adipocyte formation and elevated expression of PPARγ and LPL (Fig. 6E-L). Since skin disease and hair loss are common symptoms of SLE, these data suggest that exogenous apoEV treatment may be able to offer therapeutic potential for rescuing impaired SMSCs and HF-MSCs in SLE patients.

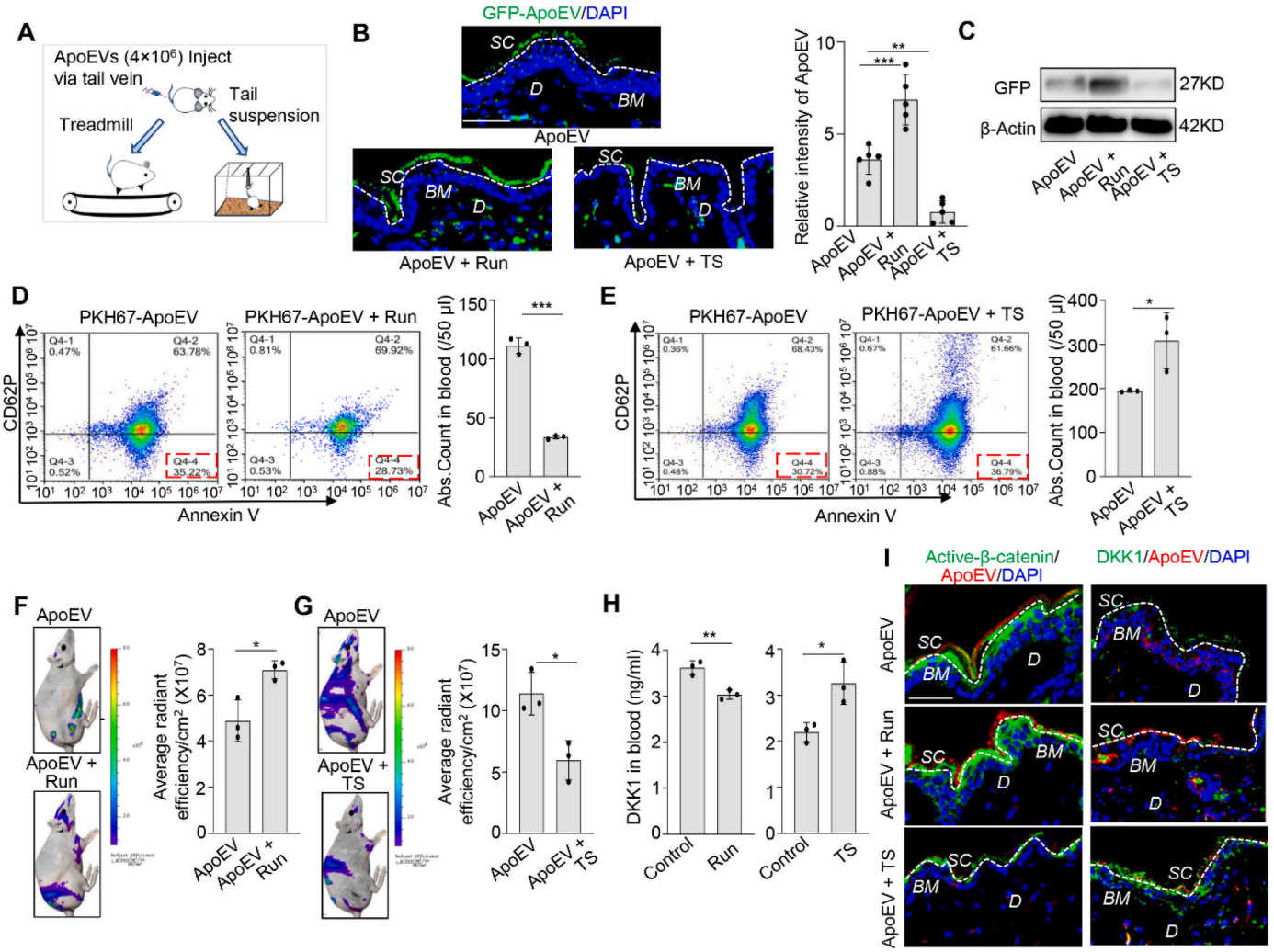

Fig. 5. Mechanical forces regulate the elimination of apoEVs through the skin. **(A)** Schematic diagram of mechanical forces applied to mice. Treadmill running exercise as a force augmentation model; tail suspension as a weightless model. **(B)** Immunofluorescent images show that the number of GFP-ApoEV migrating to the stratum corneum was increased in running group and reduced in tail-suspension group at 3 days post-injection. White dotted line represents the dividing layer between stratum corneum and the other layers of epidermis. The quantity graph shows the relative intensity of apoEVs in the skin. n = 5. **P < 0.01, ***P < 0.001, one-way ANOVA test. Data shown as mean ± SD. **(C)** Western blotting confirms the level of GFP in the skin tissue is increased in running group and reduced in tail suspension group. **(D, E)** PKH67-labeled apoEVs (4×10^6) were injected into C57BL/6 mice *via* the tail vein. After treadmill running exercise for 7 days, blood samples were collected. The flow cytometric calculation showed that the number of $PKH67^+$/Annexin V^+/$CD62P^-$ apoEVs accumulated in the blood was significantly reduced compared to the control group (D). After tail suspension for 3 days, flow cytometry analysis showed that the number of $PKH67^+$/Annexin V^+/$CD62P^-$ apoEVs in the blood was significantly increased compared to the control group (E). n = 3. *P < 0.05, Student's *t*-test. Data shown as mean ± SD. **(F, G)** DIR-labeled apoEVs (4×10^6) were injected into immunocompromised mice *via* the tail vein. *Ex vivo* fluorescent images showed that the elimination of apoEVs through the skin was increased after treadmill exercise while the migration of apoEVs through the skin was decreased after tail suspension compared to the control group, as indicated by quantitative graph. n = 3. *P < 0.05, Student's *t*-test. Data shown as mean ± SD. **(H)** ELISA analysis showed the level of DKK1 in the circulation of C57BL/6 mice was reduced after treadmill running, but enhanced after tail suspension. n = 3. *P < 0.05, **P < 0.01, Student's *t*-test. Data shown as mean ± SD. **(I)** Immunofluorescent images show the expression level of active-β-catenin (green) in skin was enhanced after treadmill running, but reduced after tail suspension. The DKK1 expression level in the skin showed opposite trends of active-β-catenin. SC, stratum corneum; BM, basement membrane; D, dermis. Scale bar (B), 50 μm; Scale bar (I), 40 μm.

2.6. *ApoEVs promote cutaneous wound healing*

Apoptosis plays an essential role in the wound healing process by inducing cell proliferation [43,44]. To examine whether MSC-derived apoEVs could promote wound healing, the mice with excision wounds were systemically injected with apoEVs or MSCs. The results showed that both apoEV and MSC infusion significantly improved wound healing from 10 to 14 days post-infusion (Figs. S6A and B). In addition, sEVs injection showed a similar capacity to promote wound healing compared with the apoEV-treated mice (Figs. S8A and B).

Previous studies showed that the Wnt/β-catenin signaling regulates the wound repair process by modulating stem cell recruitment and differentiation [45]. Our results showed that Wnt/β-catenin pathway upregulates the metabolism of apoEVs from the skin (Fig. 3D and E). To confirm the effect of Wnt/β-catenin signaling in apoEV-mediated wound healing, apoEV-treated mice were intraperitoneally injected with placebo (0.9% saline), LiCl (10 μg/g), or XAV939 (10 μg/g) at one day after wound creation. We found that administration of LiCl potentiated wound healing at 7 days post-injection compared to the apoEV-treated control group. However, administration of XAV939 slowed the wound healing process when compared to apoEV-treated control group at 3 days (P < 0.01) (Figs. S6C and D). Moreover, immunofluorescent image analysis showed that LiCl treatment increased the accumulation of PKH26-ApoEV in the wound area, whereas XAV939 reduced it

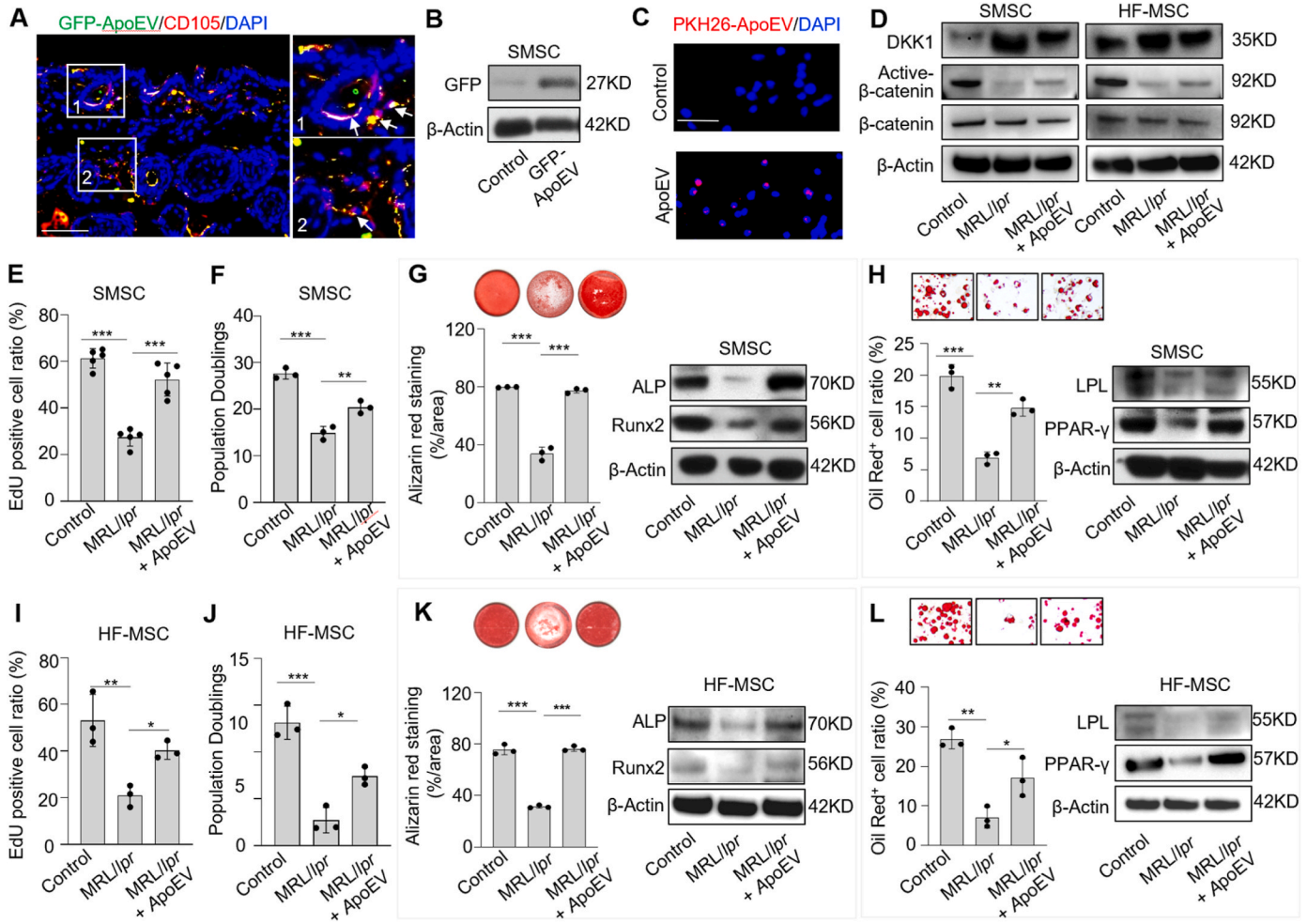

Fig. 6. ApoEV treatment improves skin and hair follicle MSC functions. **(A)** Immunofluorescent images show that GFP-ApoEV (green) were engulfed by skin MSCs (SMSCs) (1 and 2), as indicated by co-staining with CD105 at 7 days post-injection. The right panel exhibits the higher magnification of the boxed region to show colocalization of GFP-ApoEV and CD105 positive SMSCs. **(B)** Western blotting shows GFP signals was detected in SMSCs after GFP-ApoEV injection. **(C)** Immunofluorescent staining of SMSC smears shows skin cells endocytosed apoEVs. **(D)** Western blotting shows Wnt/β-catenin signaling is activated and DKK1 expression is decreased in SMSCs and hair follicle MSCs (HF-MSCs) from MRL/*lpr* mice after apoEVs injection. **(E, F, I and J)** EdU and population doubling assay show that MRL/*lpr* SMSCs and HF-MSCs had reduced proliferation and passage rates when compared to the wild-type control group. After apoEV treatment, proliferation and passage rates were improved in MRL/*lpr* SMSCs and HF-MSCs, respectively. n = 3–5. *P < 0.05, **P < 0.01, ***P < 0.001, one-way ANOVA test. Data shown as mean ± SD. **(G, K)** Compared to wild-type SMSCs, MRL/*lpr* SMSCs showed reduced capacity to form mineralized nodules when cultured under osteogenic inductive conditions, assessed by alizarin red staining, and reduced expression of osteogenic markers Runx2 and ALP, assessed by Western blotting. After apoEV treatment, reduced mineralized nodule formation and expression of Runx2 and ALP were rescued in MRL/*lpr* SMSCs (G). The osteogenic capacity of MRL/*lpr* HF-MSCs was also rescued after apoEV treatment (K). n = 3. ***P < 0.001, one-way ANOVA test. Data shown as mean ± SD. **(H, L)** Compared to wild-type SMSCs, MRL/*lpr* SMSCs showed reduced capacity to differentiate into adipocytes when cultured under adipogenic inductive conditions, as assessed by Oil red O staining, along with reduced expression of adipogenic markers PPARγ and LPL, as assessed by Western blotting. After apoEV treatment, reduced adipocyte formation and expression of PPARγ and LPL were rescued in MRL/*lpr* SMSCs (H). The adipogenic capacity of MRL/*lpr* HF-MSCs was also rescued after apoEV treatment (L). n = 3. *P < 0.05, **P < 0.01, ***P < 0.001, one-way ANOVA test. Data shown as mean ± SD. Scale bars (A, C), 50 μm.

(Fig. S6E). These results indicate that Wnt/β-catenin pathway may regulate apoEVs metabolism in the skin and affect the wound healing process.

2.7. ApoEVs promote hair regeneration

To determine whether apoEVs could induce hair growth, we examined the effect of apoEV treatment on C57BL/6 mice after clipping the dorsal hair. The hair cycle was synchronized by the depilation of telogen-phase hairs from 7-week-old C57BL/6 mice [46]. We then compared the effect of apoEVs (4×10^6) and MSCs (1×10^6) in inducing hair regrowth. Minoxidil (1%) and PBS were used as positive and negative controls, respectively. Usually, the shaved skin of C57BL/6 mice is pink during the telogen phase and darkens with anagen initiation [47]. We found that diffuse darkening of the skin after treatment with apoEVs, MSCs and Minoxidil at 7 days post-injection, but the control group displayed no significant alteration. From 7 to 14 days post-injection, the apoEV, MSC and Minoxidil groups showed significantly accelerated hair regrowth when compared to the control group (Fig. 7A and B), as assessed by H&E staining (Fig. S7A). The treatment with apoEVs increased the number ($P < 0.01$) and the length of hair follicles ($P < 0.001$) compared to the control group (Fig. S7B). Instead, sEVs exhibited no therapeutic effect for hair growth (Figs. S8C and D).

Since the Wnt/β-catenin pathway plays a key role in normal hair follicle development and cycling [48,49], we tested whether Wnt/β-catenin signaling contributes to apoEV-mediated hair regrowth. Immunohistochemistry staining showed that apoEVs, MSC, and Minoxidil treatment enhanced the expression of active-β-catenin in hair follicle compared to the control group (Fig. 7C). LiCl treatment promoted apoEV-induced expression of active-β-catenin and hair regrowth

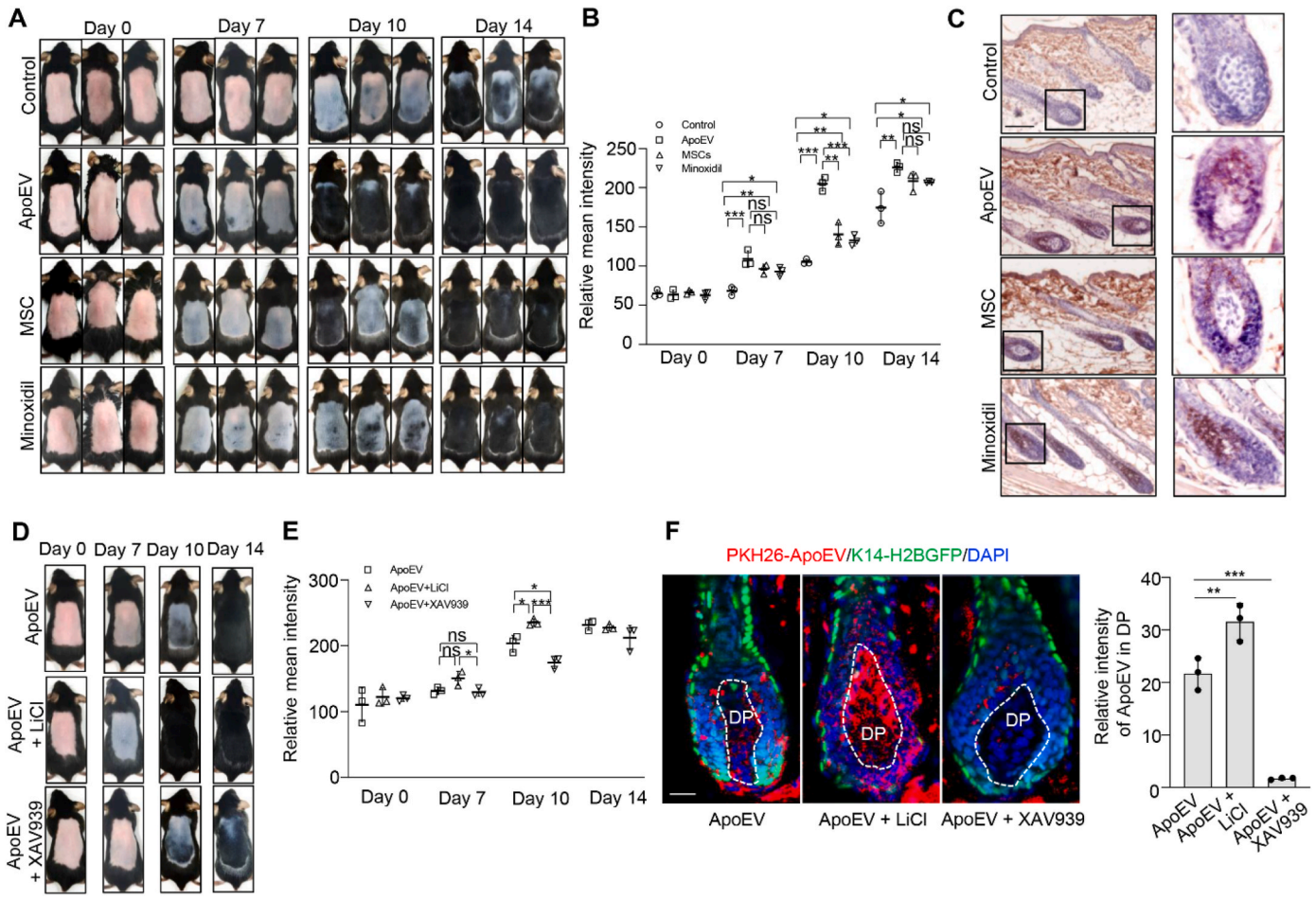

Fig. 7. ApoEVs promote hair regeneration. **(A, B)** C57BL/6 mice in the telogen phase (7 weeks old) were depilated. PBS, apoEVs (4×10^6) or MSCs (1×10^6) were subcutaneously injected into the dorsal skin. Minoxidil (1%) was topically applied daily to the dorsal skin as a positive control. Representative photos of mice showing skin color darkness and hair regrowth at 0, 7, 10 and 14 days post-injection. The level of pigmentation was quantified by the intensity of the darkness of the back skin in the same area. n = 3. *P < 0.05, **P < 0.01, ***P < 0.001, one-way ANOVA test. ns: not significant. Data shown as mean ± SD. **(C)** Immunohistochemistry staining shows the expression level of active-β-catenin in hair follicle from control, apoEV, MSC and minoxidil groups. **(D, E)** Representative photos of mice showing skin color darkness and hair regrowth after intervention at 0, 7, 10 and 14 days post-injection. The level of pigmentation was quantified by the intensity of the darkness of the back skin in the same area. n = 3. *P < 0.05, ***P < 0.001, one-way ANOVA test. ns: not significant. Data shown as mean ± SD. **(F)** Immunofluorescent images show that LiCl treatment increased the accumulation of PKH26-ApoEV in dermal papilla to promote the hair regeneration, but XAV939 treatment inhibited the accumulation of PKH26- ApoEV in dermal papilla to slow the regrowth process. White dotted line indicated the area of DP. The relative mean intensity of apoEVs around DP were calculated. n = 3. **P < 0.01, ***P < 0.001, one-way ANOVA test. Data shown as mean ± SD. DP, dermal papilla. Scale bar (C), 100 μm; Scale bar (F), 20 μm.

compared to the apoEV group at 10 days post-injection (P < 0.05), but XAV939 decreased apoEV-induced expression of active-β-catenin and the hair regeneration compared to the apoEV group (P < 0.05) (Figs. 7D, E, and S7C). Since the dermal papilla is a major control center for hair follicle growth and the hair cycle [50], we used immunofluorescent image analysis to show that LiCl treatment increased the accumulation of PKH26-positive apoEVs in the dermal papilla. However, XAV939 treatment inhibited the accumulation of PKH26-positive apoEVs in the dermal papilla (Fig. 7F). In conclusion, our experimental data reveal a previously unrecognized metabolic pathway of apoEVs and suggest a potential of using apoEVs to treat skin and hair disorders.

3. Discussion and conclusion

Apoptosis is one of the most important cell death modalities for maintaining homeostatic turnover in the body. It is believed that phagocytes are responsible for clearing apoptotic corpses to ensure a healthy, non-inflammatory environment, whereas apoptotic deficiency can lead to inflammation and various pathologies. It is estimated that each phagocyte ingests one red blood cell around every 30 min [51]. This estimation gives some perspective on the functional loading per individual phagocyte, even just considering this one cell type. From this point of view, we explored whether there is an alternative route to eliminate apoEVs. Our experimental data showed that exogenous apoEVs are metabolized in the integumentary skin and hair follicles to maintain their homeostasis. To avoid the potential off-target effect of labeling exogenous apoEVs or non-specific staining of labeling dye used in this study, we used multiple labeling approaches, including PKH26/67, GFP, DIR, and AIEgens methods to trace apoEVs metabolic paths. The migration of apoEVs is regulated by the mechanical force to nurture the skin and hair follicle tissues, indicating a potential interplay between apoptotic metabolism and tissue-specific stem cell turnover.

So far, many patients have received culture-expanded MSC transplantation to treat a variety of diseases [15,16,52]. However, the exact metabolic fate of transplanted MSCs is largely unknown. It appears that transplanted MSCs can induce recipient-derived inflammatory cell apoptosis as well as undergo self-initiated apoptosis [53–55]. MSC transplantation-associated apoptosis generates a certain number of apoEVs, resulting in immune tolerance that ameliorates autoimmune disorders. In addition, recently growing evidence shows that the

therapeutic effect of MSC transplantation may be associated with releasing extracellular vesicles containing mRNAs, regulatory miRNAs, bioactive proteins and compounds [56,57]. In this study, our experimental evidence suggests that apoEVs, an important apoptotic metabolite, are cleared through the integumentary system.

Parabiosis models have been applied to study circulating factors between two organisms [58]. We used this system in our previous study to demonstrate that apoEVs participate in the circulation to modulate bone marrow MSCs [11]. To identify the metabolism of circulating apoEVs, we generated a parabiosis mouse model, in which GFP and WT mice were surgically joined to share the circulation system through the microvasculature, as described in our previous report [11]. Using the same approach, it was reported that biological molecules in the circulation could be transmitted from a young mouse to an old mouse to rejuvenate an aged organ system [59]. In this study, we observed that the natural cell-derived apoEVs from GFP mice were eliminated from the stratum corneum and hair follicles after heterochronic parabiosis, suggesting metabolism of apoEVs through integumentary system may be a common biological event.

The skin epidermis is regularly renewed throughout life. IFE cells continuously proliferate and differentiate to form a cornified layer that is continuously shed, while HFs undergo cycles of degeneration and regeneration. Both processes require the activation of epidermal stem cells (SCs), located in the basal layer of the IFE and the outer layer of the bulge in the HF. Wnt/β-catenin signaling plays crucial roles in the maintenance, activation, and fate determination of the SC populations [33]. Loss of Wnt/β-catenin in postnatal dermal papilla or epithelia, cause failure of matrix cell proliferation and premature catagen [60,61]. Wnt/β-catenin signaling contribute to progenitor cell proliferation in non-hairy epithelia and IFE under homeostatic conditions [32]. Therefore, activation of Wnt/β-catenin pathway will accelerate the elimination of apoEVs through promoting cell proliferation and exfoliation of the skin and hair. We found the biodistribution of apoEVs in the skin is closely associated with the expression level of Wnt/β-catenin. However, the mechanism is unclear and should be further investigated in the future.

Cells in all multicellular organisms are exposed to mechanical forces through adhesion to neighboring cells and to the extracellular matrix (ECM), as well as the ebb and flow of the environment. In this study, we found that the pattern of apoEV elimination from the skin exhibited a wave-like pattern, suggesting this process may be regulated by mechanical force. On the other hand, the generation of multi-layer wave-like pattern from the basal membrane to stratum corneum may be partly due to the structure characteristics of epidermis. During treadmill exercise, organisms experience mechanical power from muscles [62,63]. Tail suspension of mice is a typical mechanical unload model, which has been widely used to simulate the effects of spaceflight and microgravity environments [64,65]. It is known that mechanical force may regulate the Wnt/β-catenin pathway. The level of DKK1 in serum is reduced after exercise [66–69], but tends to increase in the tibia after tail suspension [70]. We found the level of DKK1 in serum was decreased after treadmill exercise and enhanced after tail suspension, suggesting mechanical force regulates the Wnt/β-catenin pathway to control the elimination of apoEVs through DKK1. Besides, the altered blood distribution may have effect on EV biodistribution.

Apoptotic deficiency can cause autoimmune diseases such as systemic lupus erythematosus (SLE) [71,72], in which the healthy tissue and organs are mistakenly attacked by the immune system. MRL/*lpr* mice are an apoptosis-associated SLE model with Fas mutation, and exhibit skin lesions, hair loss, and osteopenia [11,42,73]. Our previous study showed that apoEVs could rescue impaired bone marrow MSCs in MRL/*lpr* mice *via* regulating the Wnt/β-catenin pathway [11]. Here, we found the SMSCs and HF-SMCs are also capable of engulfing exogenous apoEVs to activate the Wnt/β-catenin pathway and rescue impaired stem cell function in MRL/*lpr* mice, indicating that accumulation of apoEVs in the skin not only eliminates metabolites but also nurtures the skin and hair follicle stem cells.

EVs can be generally categorized into the sEVs (30–150 nm), microvesicles (100–1000 nm), and apoEVs (50–5000 nm) based on their size, density, morphological features, content, and biogenesis. According to the latest statement of ISEV, biogenesis is one of the most important distinguishing factors between apoEVs and sEVs [74]. The inward budding of endosomal membrane generates numerous accumulations of intraluminal vesicles (ILV) within MVB, which are released into the extracellular environment by fusion of plasma membrane with MVBs, referred to as sEVs [75]. ApoEVs are formed through the outward budding of the plasma membrane during apoptosis [9]. Whereas sEVs are secreted during normal cellular processes, apoEVs are formed only during programmed cell death. ApoEVs and sEVs both possess a lipid bilayer membrane, containing protein, lipids and genetic materials. Although the exact physiological functions of EVs are not fully elucidated, apoEVs and sEVs can serve as kind transport vehicles, exerting their diverse biological functions [76]. In this study, our Western blotting results confirmed apoEVs from mouse BMMSCs expressed β-Actin but sEVs from mouse BMMSCs failed to express β-Actin, consistent with previous report [77].

Cutaneous wound healing is a process comprising four phases to restore the injured skin: homeostasis, inflammatory, proliferative and remodeling phases [78]. Wnt/β-catenin signaling is activated by wounding and involved in the whole healing process from the control of inflammation and cell apoptosis to the migration of stem cell reservoirs within the wound site [79]. Multiple roles of EVs in boosting wound healing have been identified, including enhancing cell proliferation, activating migration, stimulating angiogenesis and ameliorating scarring [80,81]. MSC-derived exosomes can improve wound re-epithelialization and cell proliferation by activation of Wnt/β-catenin signaling, and knockdown of Wnt4 in MSC-derived exosomes reduces the therapeutic effects both *in vitro* and *in vivo* [82]. During wound healing, keratinocytes migrate from wound edge or other epidermal reservoir areas to regenerate epidermis for wound closure [83,84]. We found that apoEV treatment not only elevated active-β-catenin expression in mesenchymal stem cells but also in keratinocytes, which may jointly accelerate wound healing process [33,79].

Hair follicle cycling is a dynamic and complex process involving alternating phases of rapid growth (anagen), regression (catagen), and quiescence (telogen) [85]. Activation of Wnt/β-catenin signaling in dermal papilla (DP) cells is crucial for hair growth [50,86,87]. Hair loss, induced by dysregulation of hair cycling, is caused by various factors associated with the environment, genetics, hormones and aging [88,89]. Current drug treatments such as minoxidil provide only short-term improvement, and hair regrowth may be impaired after discontinuation of the drug [90]. MSC therapy improves hair regrowth by regulating Wnt/β-catenin signaling in DP cells and secreting growth factors [91,92]. EVs derived from MSCs and macrophages can activate DP cells and increase Wnt/β-catenin pathway activity in the skin to promote hair regeneration [93–95]. In this study, we showed that both apoEVs and sEVs can improve wound healing process. Whereas, apoEVs, but not sEVs, accelerate hair regeneration, which may be due to different vesicle contents between apoEVs and sEVs. Here, we provide direct evidence to identify a route through which apoptotic metabolites are eliminated and show that apoEVs activate Wnt/β-catenin signaling in the skin to improve SMSC and HF-MSC functions in MRL/*lpr* mice.

4. Materials and methods

4.1. Mice

Female C57BL/6-Tg (CAG-EGFP)1Osb/J and C3MRL-Fas^{lpr}/J (MRL/*lpr*) mice were purchased from the Jackson Laboratory. Female immunocompromised mice (BALB/c-nu/nu) were purchased from the Sun Yat-sen University, Guangzhou, China. Female C57BL/6J mice were purchased from Sebiona company. K14–H2BGFP mice were kindly

provided by Dr. Chen of the National Institutes of Biological Sciences (Beijing, China). All animal experiments were performed under institutionally approved protocols for the use of animal research (Sun Yat-sen University SYSU-IACUC #2020–000407 and University of Pennsylvania IACUC #805478).

4.2. Reagents and antibodies

Staurosporine (ALX-380-014) was purchased from Enzo Life Sciences (Farmingdale, NY, USA). XAV939 (13596) was purchased from Cayman Chemical (Ann arbor, MI, USA). Lithium chloride (14540) was purchased from Alfa Aesar (Tewksbury, MA, USA). PKH26 (MINI26) and PKH67 (MINI67) cell linker were purchased from Sigma (St. Louis, MO, USA). DIR (C019) was purchased from ABP Biosciences (Rockville, MD, USA). Cell mask™ Deep Red plasma membrane stain (C10046) was purchased from Thermo Fisher Scientific (Waltham, MA, USA). EdU staining kit (Code No. KGA331-1000) was purchased from KeyGEN BioTECH (Nanjing, China). EdU regent (C00052), Cell-Light™ Apollo567 Stain Kit (100T) (Code No. C10371-1) and Cell-Light™ Apollo643 Stain Kit (100T) (Code No. C10371-2) were purchased from RIBOBIO CO., LTD (Guangzhou, China). DPPS liposomes containing 2% Cy3 were purchased from the Ruixi Biological Technology Co., LTD (Xi'an, China). Phalloidin for actin staining (green and red) were purchased from BioLegend (San Diego, CA, USA).

Anti-mouse Runx2 (8486), anti-rabbit Calreticulin (12238) and anti-rabbit Caspase 3 (9662) was purchased from Cell Signaling Technology (Danvers, MA, USA). Anti-rabbit CD9 (ab92726), anti-rabbit TSG101 (ab125011), anti-rabbit Syntenin (ab19903) and anti-rabbit Lamin B1 (ab133741) were purchased from Abcam (Cambridge, MA, USA). Alexa Fluor 488, Alexa Fluor 568 and Alexa Fluor 647 antibodies were purchased from Invitrogen (Carlsbad, CA, USA). Anti-mouse ALP (sc-28904), anti-mouse PPARγ (sc-7273) and anti-mouse β-catenin (sc-7963) were purchased from Santa Cruz Biotechnology (Santa Cruz, CA, USA). Anti-mouse LPL (SAB2700761) and anti-β-actin antibody (A1978) were purchased from Sigma (St. Louis, MO, USA). Annexin V-APC (10040–11) were purchased from Southern Biotech (Birmingham, AL, USA). CD62P-PE (12–0626) was purchased from eBioscience (San Diego, CA, USA). Annexin V-FITC (556419) and 7AAD (559925) were purchased from BD Biosciences. Anti-mouse active-β-catenin (05665) was purchased from EMD Millipore (Billerica, MA, USA). Anti-rabbit GFP (NB600-308) was purchased from Novus Biologicals (Centennial, CO, USA). Anti-rabbit DKK1 (AF4600) was purchased from Affinity Biosciences (Jiangsu, China).

4.3. Isolation and characterization of apoEVs

When MSCs reached full confluency, cells were washed with PBS and the culture medium was substituted with a basic medium containing 500 nM STS without FBS. After undergoing apoptosis for 16 h, apoEVs were isolated and purified using sequential centrifugation followed by sequential filtering. Briefly, after 800×*g* centrifugation for 10 min and 2000×*g* centrifugation for 10 min to remove cell debris, the supernatant was subsequently filtered with 5 μm filters to collect the supernatant containing particles less than 5 μm in diameter. Next, the supernatant was centrifuged at 16000×*g* for 30 min to pellet the apoEVs (Fig. 1A).

For labeling of apoEVs with AIEgens, DCPy was synthesized according to our established protocol [26]. DCPy was added to the serum-free cell culture medium at a final concentration of 5 μM and incubated for 30 min. Subsequently, cells were induced apoptosis by ultralow-power light irradiation at 0.7 mW/cm^2 for 6 h.

The morphology of apoEVs was observed with TEM. ApoEVs pellets were resuspended in 1% glutaraldehyde for 30 min. Samples were dripped on Formvar-coated copper grids and incubated for 20 min. After washing, samples were negatively stained with 2.5% uranyl acetate for 2 min. Images were performed using a JEM-1200EX TEM (JEOL, Japan).

For nanoparticle tracking analysis, apoEVs were diluted in filtered PBS. The particle size was measured with ZetaView PMX120 (Particle Metrix, Germany). Data were analyzed using the ZetaView software 8.02.31.

Furthermore, apoEVs were diluted in PBS and analyzed using nanoflow cytometry (Flow NanoAnalyzer, NanoFCM Inc.) according to the manufacturer's protocol [96]. The samples were diluted resulting in a particle count within the optimal range of 4000–14,000. Particle concentration and size distribution were calculated using the NanoFCM software (NanoFCM Profession V1.0). To analyze the proportion of fluorescent intensity, apoEVs were stained with Annexin V-FITC, Calreticulin or Lamin B1 antibodies, followed by secondary antibody staining.

4.4. Isolation of small EVs

When MSCs reached 80% confluency, cells were washed with PBS and culture media supplemented with 5% exosomes-depleted FBS (SBI) was replaced. After 40 h, culture supernatant was collected and centrifuged at 800×*g* for 10 min and 2000×*g* for 10 min to remove cellular debris. Subsequently, the supernatant was centrifuged at 16000×*g* for 30 min to remove medium EVs and at 120000×*g* for 2 h to get sEVs.

4.5. TUNEL assay

After treatment with STS for 16 h, MSCs were fixed with 4% PFA and permeabilized. According to the manufacture's protocol, cells were incubated with TUNEL reagent (G3250, Promega) for 60 min at 37 °C. Positive cells were counted after counterstained with DAPI under microscope.

4.6. Flow cytometry analysis

To evaluate the apoptosis rate of apoptotic cells, cells were suspended in 1 × Annexin V binding buffer and incubated with Annexin V-FITC and 7AAD for 15 min at room temperature. After the same volume of 1 × Annexin V binding buffer was added to stop the reaction, apoptosis was analyzed by flow cytometry (NovoCyte, ACEA Biosciences, USA). To examine the number of exogenous apoEVs after treadmill exercise or tail suspension, PKH67 labeled apoEVs were systemically injected via tail vein and isolated from the blood samples. ApoEVs were stained with 1 μg of CD62P-PE antibodies on ice for 30 min. ApoEVs were pelleted and stained with 1 μg of Annexin V-APC in binding buffer. ApoEVs were defined as Annexin V-positive and CD62P-negative events.

4.7. Isolation of mouse bone marrow, skin and hair follicle MSCs

MSCs from bone marrow and skin were isolated and cultured as in our previous reports [11,21]. Skin tissues from mice were gently separated, minced and digested with solution containing collagenase type I (2 mg/ml; Worthington Biochemical) and dispase II (4 mg/ml; Roche Diagnostics) in phosphate-buffered saline (PBS) for 1 h at 37 °C. Bone marrow cells were flushed out from mouse femurs and tibias with 2% heat-inactivated fetal bovine serum (FBS, RMBI, Missoula, MT, USA) in PBS. Single-cell suspensions from the skin or bone marrow were obtained by passing the cells through a 70 μm strainer (BD Biosciences). All nucleated cells were seeded on 10 cm culture dish (Corning, NY, USA) at 37 °C in 5% CO_2. Non-adherent cells were removed after 48 h and attached cells were maintained for 12 days in alpha minimum essential medium (α -MEM, BI, Cromwell, CT, USA) supplemented with 20% FBS, 2 mM L-glutamine, 55 μM 2-mercaptoethanol, 100 U/mL penicillin and 100 μg/mL streptomycin (Invitrogen). These single colonies were passaged with frequent medium changes to eliminate potential hematopoietic cell contamination. Colony-forming attached cells were passed once for further experimental use. Hair follicle MSCs were isolated followed a previously reported protocol [97,98]. Briefly,

7-week-old MRL/*lpr* female mice were sacrificed with ketamine/xylazine injection followed by cervical dislocation. The lip pads containing vibrissae were removed with scissors and placed in PBS with 200 U/mL penicillin and 200 μg/mL streptomycin (Invitrogen). Under a dissecting microscope, forceps and scissors were used to remove the subcutaneous fat and connective tissue to expose the rows of vibrissae. Individual vibrissae were separated by pulling away from the pad using fine forceps. The matrix component was then removed, and any epithelial tissue still present on the papilla was teased off. The end bulb was then dissected and transferred to a 35 mm dish. Extracted papillae were cultured in complete culture medium as described for isolation of SMSCs and BMMSCs at 37 °C in 5% CO_2. After 5 days, medium was changed twice a week. When primary cell confluence reached 80%, the cells were passaged to a 60 mm culture dish (Corning, NY, USA) and FBS was reduced to 10%.

4.8. Cell proliferation assay

5-ethynyl-2′-deoxyuridine (EdU) incorporation assay was used to evaluate the proliferation of MSCs. Briefly, passage 2 (P2) MSCs (1.0×10^4 cells/well) were seeded on 2-well chamber slides (Nunc) and cultured for 2–3 days. EdU solution (KeyGEN BioTECH) was added at final concentration 50 μM in the medium and cells were subsequently cultured for 2h. The cells were stained with a EdU staining kit (KeyGEN BioTECH) according to the manufacturer's instructions. Cell proliferation capacity was shown as a percentage of EdU-positive nuclei over total nucleated cells. The EdU assay was repeated in three independent samples for each experimental group.

4.9. Population doubling (PD) assay

Single colony cluster cells (P0 cells) were digested using trypsin and seeded at 0.5×10^6 on a 60 mm dish (Corning). When the cells reached sub-confluence, they were harvested and seeded at the same density. These steps were repeated until the cells lost dividing capability. The PD score was calculated at every passage according to the equation: PD = $\log_2$ (number of final cells/number of initiated seeded cells). The total scores were determined by cumulative addition of total numbers generated from each passage. The PD assay was repeated with three independent isolated cells for each experimental group.

4.10. Osteogenic differentiation assay

MSCs were seeded at 1×10^6 cells per well onto a 6-well plate. When they reached 100% confluence and stopped proliferating, cells were induced with osteogenic medium containing 100 μM L-ascorbic acid 2-phosphate (Sigma), 2 mM β-glycerophosphate (Sigma) and 10 nM dexamethasone (Sigma). Seven days after osteogenic induction, total protein was extracted from cultured MSCs and the expression of Runx2 and ALP was analyzed by Western blotting. The cultures were stained with 1% alizarin red-S (Sigma) after four weeks of osteogenic induction. Alizarin red-positive area was analyzed using Image-J software (NIH) and shown as a percentage of the total area.

4.11. Adipogenic differentiation

MSCs were seeded at 1 × 106 cells per well onto a 6-well plate. When the cells reached 100% confluence and stopped proliferating, they were induced with adipogenic medium containing 500 nM hydrocortisone (Sigma-Aldrich), 500 nM isobutylmethylxanthine (Sigma-Aldrich), 100 nM L-ascorbic acid phosphate, 10 μg/mL insulin (Sigma-Aldrich) and 60 μM indomethacin (Sigma-Aldrich). Seven days after the induction, total protein was extracted from cultured MSCs and the expression of PPARγ and LPL was analyzed by Western blotting. At 21 days post-induction, the cultures were stained with Oil red O (Sigma-Aldrich), and positive cells were quantified under microscopy and shown as a percentage of the total number of cells.

4.12. Western blot analysis

Total protein was extracted using M-PER mammalian protein extraction reagent (Thermo, Rockford, IL, USA). Twenty μg of proteins were separated on 4%–12% NuPAGE BT gel (Invitrogen) and transferred to 0.2 μm nitrocellulose membranes (Millipore, Bedford, MA, USA). The membranes were blocked with 5% non-fat dry milk and 0.1% tween 20 for 1 h, followed by incubation with the primary antibodies (1:200–1000 dilution) at 4 °C overnight. The membranes were then incubated at room temperature for 1 h in species-related horseradish peroxidase–conjugated secondary antibody (Santa Cruz Biotechnology) diluted at 1:10,000 in blocking solution. The immunoreactive proteins on the membranes, enhanced by SuperSignal West Pico Chemiluminescent Substrate (Thermo), were detected by ChemiDoc™ MP imaging system (BIO-RAD). β-Actin antibody was used to quantify the amount of loaded protein.

4.13. Ex vivo apoEVs distribution analysis

ApoEVs (4×10^6) were labeled with 20 μl DIR (1 mM). The labeled nanoparticles were suspended in 200 μL PBS and infused into BALB/c-nu/nu mice through the tail vein. PBS was used as a negative control. At a set time point, the time-dependent biodistribution of the DIR-apoEVs in the mice was imaged using an IVIS spectrum imaging system (PerKin Elmer). At designated time intervals after injection with DIR-apoEVs, the mice were sacrificed. Skin and the main organs (heart, liver, spleen, lungs, kidneys) were isolated, and *ex vivo* fluorescence imaging was performed using the imaging system. The signals were collected in the 745 nm channel with laser excitation at 800–820 nm. The intensity of fluorescence signals was quantified by average radiance from a fixed-area region of interest (ROI) over the target organ.

4.14. Immunofluorescent staining

ApoEVs or MSCs were stained with PKH26 and infused into C57/BL6, MRL/*lpr*, or K14–H2BGFP mice. At the set time point, skin or other tissues were collected and fixed in 4% PFA, followed by embedding in OCT compound (Sakura Finetek, Torrance, CA, USA). Frozen sections were prepared and slides were stained with GFP, active-β-catenin, CD105 or Lamin B1 antibodies, followed by secondary antibody staining. Finally, slides were mounted with Vectashield mounting medium containing DAPI and observed under the confocal microscope. To detect surface markers, apoEVs were incubated with Annexin V-FITC for 15 min at room temperature, Calreticulin or Lamin B1 antibodies for 1 h at 4 °C, followed by secondary antibody staining. Counterstained with Cell mask, apoEVs were placed on the slides and observed immediately. To detect *in vivo* engulfment of apoEVs by SMSC, PKH26-labeled apoEVs were injected into MRL/*lpr* mice through the tail vein. At 7 days post-infusion, the skins were excised and digested with solution containing collagenase type I (2 mg/ml; Worthington Biochemical) and dispase II (4 mg/ml; Roche Diagnostics) in phosphate-buffered saline (PBS) for 1 h at 37 °C. After 1500 × rpm centrifugation for 5 min, cell smears were placed on the slides, mounted with Vectashield mounting medium containing DAPI and observed under the confocal microscope. Images were performed by a Zeiss LSM 900 confocal microscope or Zeiss Elyra 7 with Lattice SIM and analyzed using the Zen 2.3 SP1 software, Blue Edition.

4.15. Immunohistochemistry staining

Paraffin-embedded skin sections were dewaxed and hydrated. For antigen retrieval, slides were boiled in 10 mM sodium citrate buffer and then maintained at a sub-boiling temperature for 10 min. To block endogenous peroxidase activity, sections were incubated in 3%

hydrogen peroxide for 15 min in room temperature. After washing with PBS, the slides were blocked with blocking buffer for 1 h and incubated with anti-active-β-catenin (1:100) antibody overnight at 4 °C. After washing, slides were incubated with biotinylated secondary antibody (sc-516142) (1:200) for 1 h at 37 °C. After incubating with HRP-streptavidin complex (PK-6100, VECTOR) for 30 min, slides were developed until light brown staining was visible with DAB chromogen kit (SK-4100, VECTOR).

4.16. Parabiosis model

The mice were anaesthetized and shaved along the opposite lateral flanks. The excess hair was wiped off with an alcohol prep pad. After further disinfection with Betadine solution and 70% alcohol, identical incisions were made on the corresponding lateral aspects from the olecranon to the knee joint of each mouse. The olecranon and knee joints were each attached by a single 4-0 silk suture and tie, and the dorsal and ventral skins were sewn together with continuous 5-0 Vicryl suture. The mice were then kept on heating pads and continuously monitored until full recovery. Buprenorphine was used for analgesic treatment by subcutaneous injection every 8–12 h for 48 h after the operation.

4.17. In vivo imaging by two-photon laser-scanning microscopy (TPLSM)

The whole procedure was performed according to a previous report [99]. Three-week-old K14–H2BGFP mice were anaesthetized with intraperitoneal injection of ketamine and xylazine, and the skin around the head region was shaved using a mechanical trimmer and depilatory cream. PKH26-labeled apoEVs (4×10^6) were subcutaneously injected into the shaved area. The mouse was placed on a heated stage and kept anaesthetized with vaporized isoflurane through a gas tube connected to the head. The injected area was immobilized by a vacuum extractor and imaged directly under a water lens. Image stacks of the skin were acquired with a FVMPE-RS (Olympus) microscope equipped with a two-photon laser. A laser beam (with a wavelength of 920 nm for GFP and 1040 nm for PKH26) was focused through a 20X water lens. Serial optical sections were acquired to image the layer of stratum corneum at 3 min intervals for a total of 30 min.

4.18. EdU labeling in vivo

Mice were injected intraperitoneally with EdU (10 mg/kg) in PBS and skins were harvested at designed time points. Collected tissues were fixed in 4% PFA, followed by embedding in OCT compound (Sakura Finetek, Torrance, CA, USA). Frozen section slides were stained with Cell-Light™ Apollo567 Stain Kit (RIBOBIO) or Cell-Light™ Apollo643 Stain Kit (RIBOBIO) according to the manufacturer's protocol. Sections were counterstained with Hoechst and mounted for fluorescence microscopy analysis.

4.19. Treadmill exercise

Mice were divided into two treatment groups, one subjected to exercise and one staying sedentary. The mice in the exercise group were trained for one week with a lower speed to adapt to the exercise. After training, mice experienced daily exercise consisting of 30 min treadmill running at a speed of 7.0 m/min with no inclination of the 8-lane treadmill (SA101C, SANS, CHINA). The mice were motivated by a small stick or by transient electric stimulation incorporated into the treadmill. At the designed time point, blood samples and skin were collected for ELISA, flow cytometry, immunofluorescent staining and intravital imaging analysis.

4.20. Tail suspension

Mice were outfitted with tail harnesses and suspended in customized cages. The mice could move within the cage using their forelimbs, which remained in contact with the cage floor, but their hindlimbs remained suspended in air and consequently failed to generate ground reaction forces. Food and water were provided on the cage floor. At the designed time point, blood samples and skin were collected for ELISA, flow cytometry, immunofluorescent staining and intravital imaging analysis.

4.21. Enzyme-linked immunosorbent (ELISA) assay

Blood samples were collected after treadmill exercise or tail suspension. DKK1 was measured with ELISA kits from R&D Systems (Minneapolis, MN, USA) according to the manufacturer's instructions.

4.22. Wound healing

Cutaneous wounds were created according to a previous report [21]. Seven-week-old C57BL/6 mice were anaesthetized and the dorsal skin was shaved using a mechanical trimmer and depilatory cream. The skin on the midback of each mouse was marked, lifted and excised to create a full-thickness wound (1 cm × 1 cm). The mice were systemically injected with PBS, MSCs (1×10^6), apoEVs (4×10^6) or sEVs (4×10^6). One day after wound creation, the mice were intraperitoneally injected with placebo (0.9% saline), LiCl (10 μg/g) or XAV939 (10 μg/g) once every three days. To check for the accumulation of apoEVs in the wound area, apoEVs (4×10^6) were labeled with PKH26, followed by immunofluorescent staining. The changes in the cutaneous wounds were recorded by a series of digital photographs, containing a ruler for scale. At the indicated time points, the percentage of wound closure was quantified on photographs using Image J software. The wound healing effects were expressed as a percentage of wound area at the measured time point over the initial wound area.

4.23. Hair regeneration

Dorsal skin hairs in the telogen phase from 7-week-old C57BL/6 mice were depilated with an animal clipper and wax. PBS, apoEVs (4×10^6) or MSCs (1×10^6) were subcutaneously injected into the dorsal skin as well as sEVs (4×10^6). 1% Minoxidil was topically applied daily to the dorsal skin as a positive control. One day after apoEV injection, the mice were intraperitoneally injected with placebo (PBS), LiCl (10 μg/g) or XAV939 (10 μg/g) every three days. To check for the accumulation of apoEVs in the hair follicle, apoEVs (4×10^6) were labeled with PKH26. Images of each animal were captured after 0, 7,10 and 14 days, and the level of pigmentation was quantified by the intensity of the darkness of the back color in the same area using ImageJ software. The mice were sacrificed at set time points and skin tissues were obtained for further histological analysis and immunofluorescent staining.

4.24. Statistical analysis

Data are presented as means ± SD of at least triplicate measurements. Comparisons between two groups were analyzed using independent unpaired two-tailed Student's t-tests, and comparisons between more than two groups were analyzed using one-way ANOVA. P values less than 0.05 were considered statistically significant. Graph analysis was performed using GraphPad Prism 8.00 (GraphPad Software, USA).

General

We appreciate all members of the Shi lab for support and helpful scientific discussion. We thank Dr. Ting Chen in the National Institutes of Biological Sciences for providing K14–H2BGFP mice.

Funding details

This work was supported by grants from the National Key R&D

Program of China (2021YFA1100600 to S.S.), the Guangdong Financial Fund for High-Caliber Hospital Construction (174-2018-XMZC-0001-03-0125, D-07 to S.S., D-11 to X.K.), the Pearl River Talent Recruitment Program (2019ZT08Y485), the National Science and Technology Major Project of the Ministry of Science and Technology of China (2018ZX10302207-001-002), the Sun Yat-sen University Young Teacher Key Cultivation Project (18ykzd05 to X.K.), the Natural Science Foundation of Guangdong (2016A030313262 to X.M.), the National Natural Science Foundation of China (82170924 to X.K., 81700928 to L.M.) and the Youth Teacher Training Project of Sun Yat-sen University (17ykpy71 to L.M.).

Data and materials availability

K14–H2BGFP mice are obtained under an MTA from the Rockefeller University. All other data are available in the manuscript and supplementary materials.

Declaration of competing interest

The authors declare that they have no competing interests.

CRediT authorship contribution statement

Lan Ma: Conceptualization, Formal analysis, Investigation, Writing – original draft, Funding acquisition. **Chider Chen:** Formal analysis. **Dawei Liu:** Formal analysis. **Zhiqing Huang:** Investigation, Validation. **Jiaqi Li:** Investigation, Validation. **Haixiang Liu:** Methodology. **Ryan Tsz Kin Kwok:** Methodology. **Benzhong Tang:** Methodology. **Bingdong Sui:** Formal analysis. **Xiao Zhang:** Formal analysis. **Jianxia Tang:** Formal analysis. **Xueli Mao:** Formal analysis, Funding acquisition. **Weiying Huang:** Resources. **Songtao Shi:** Conceptualization, Writing – review & editing, Supervision, Project administration, Funding acquisition. **Xiaoxing Kou:** Conceptualization, Writing – review & editing, Supervision, Project administration, Funding acquisition.

Declaration of competing interest

Authors declare no competing interests.

Appenix A. Supplementary data

Supplementary data to this article can be found online at https://doi.org/10.1016/j.bioactmat.2022.04.022.

References

[1] J.F. Kerr, A.H. Wyllie, A.R. Currie, Apoptosis: a basic biological phenomenon with wide-ranging implications in tissue kinetics, Br. J. Cancer 26 (4) (1972) 239–257.
[2] M.P. Baar, R.M.C. Brandt, D.A. Putavet, J.D.D. Klein, K.W.J. Derks, B.R. M. Bourgeois, S. Stryeck, Y. Rijksen, H. van Willigenburg, D.A. Feijtel, I. van der Pluijm, J. Essers, W.A. van Cappellen, I.W.F. van, A.B. Houtsmuller, J. Pothof, R.W. F. de Bruin, T. Madl, J.H.J. Hoeijmakers, J. Campisi, P.L.J. de Keizer, Targeted apoptosis of senescent cells restores tissue homeostasis in response to chemotoxicity and aging, Cell 169 (1) (2017) 132–147, e16.
[3] Y. Fuchs, H. Steller, Programmed cell death in animal development and disease, Cell 147 (4) (2011) 742–758.
[4] I.K. Poon, Y.H. Chiu, A.J. Armstrong, J.M. Kinchen, I.J. Juncadella, D.A. Bayliss, K. S. Ravichandran, Unexpected link between an antibiotic, pannexin channels and apoptosis, Nature 507 (7492) (2014) 329–334.
[5] G.K. Atkin-Smith, R. Tixeira, S. Paone, S. Mathivanan, C. Collins, M. Liem, K. J. Goodall, K.S. Ravichandran, M.D. Hulett, I.K. Poon, A novel mechanism of generating extracellular vesicles during apoptosis via a beads-on-a-string membrane structure, Nat. Commun. 6 (2015) 7439.
[6] G.K. Atkin-Smith, I.K.H. Poon, Disassembly of the dying: mechanisms and functions, Trends Cell Biol. 27 (2) (2017) 151–162.
[7] Michael R. Elliott, Kodi S. Ravichandran, The dynamics of apoptotic cell clearance, Dev. Cell 38 (2) (2016) 147–160.
[8] S. Arandjelovic, K.S. Ravichandran, Phagocytosis of apoptotic cells in homeostasis, Nat. Immunol. 16 (9) (2015) 907–917.
[9] S. Caruso, I.K.H. Poon, Apoptotic cell-derived extracellular vesicles: more than just debris, Front. Immunol. 9 (2018) 1486.
[10] M.R. Muhsin-Sharafaldine, B.R. Kennedy, S.C. Saunderson, C.R. Buchanan, A. C. Dunn, J.M. Faed, A.D. McLellan, Mechanistic insight into the procoagulant activity of tumor-derived apoptotic vesicles, Biochim. Biophys. Acta Gen. Subj. 1861 (2) (2017) 286–295.
[11] D. Liu, X. Kou, C. Chen, S. Liu, Y. Liu, W. Yu, T. Yu, R. Yang, R. Wang, Y. Zhou, S. Shi, Circulating apoptotic bodies maintain mesenchymal stem cell homeostasis and ameliorate osteopenia via transferring multiple cellular factors, Cell Res. 28 (9) (2018) 918–933.
[12] C.B. Medina, P. Mehrotra, S. Arandjelovic, J.S.A. Perry, Y. Guo, S. Morioka, B. Barron, S.F. Walk, B. Ghesquiere, A.S. Krupnick, U. Lorenz, K.S. Ravichandran, Metabolites released from apoptotic cells act as tissue messengers, Nature 580 (7801) (2020) 130–135.
[13] D. Raj, D.E. Brash, D. Grossman, Keratinocyte apoptosis in epidermal development and disease, J. Invest. Dermatol. 126 (2) (2006) 243–257.
[14] R. Kakarla, J. Hur, Y.J. Kim, J. Kim, Y.J. Chwae, Apoptotic cell-derived exosomes: messages from dying cells, Exp. Mol. Med. 52 (1) (2020) 1–6.
[15] L. Sun, K. Akiyama, H. Zhang, T. Yamaza, Y. Hou, S. Zhao, T. Xu, A. Le, S. Shi, Mesenchymal stem cell transplantation reverses multiorgan dysfunction in systemic lupus erythematosus mice and humans, Stem Cell. 27 (6) (2009) 1421–1432.
[16] K. Le Blanc, I. Rasmusson, B. Sundberg, C. Götherström, M. Hassan, M. Uzunel, O. Ringdén, Treatment of severe acute graft-versus-host disease with third party haploidentical mesenchymal stem cells, Lancet 363 (9419) (2004) 1439–1441.
[17] A. Augello, R. Tasso, S.M. Negrini, R. Cancedda, G. Pennesi, Cell therapy using allogeneic bone marrow mesenchymal stem cells prevents tissue damage in collagen-induced arthritis, Arthritis Rheum. 56 (4) (2007) 1175–1186.
[18] J. Liang, H. Zhang, B. Hua, H. Wang, J. Wang, Z. Han, L. Sun, Allogeneic mesenchymal stem cells transplantation in treatment of multiple sclerosis, Mult. Scler. 15 (5) (2009) 644–646.
[19] K. Xuan, B. Li, H. Guo, W. Sun, X. Kou, X. He, Y. Zhang, J. Sun, A. Liu, L. Liao, S. Liu, W. Liu, C. Hu, S. Shi, Y. Jin, Deciduous autologous tooth stem cells regenerate dental pulp after implantation into injured teeth, Sci. Transl. Med. 10 (455) (2018).
[20] C. Zheng, B. Sui, X. Zhang, J. Hu, J. Chen, J. Liu, D. Wu, Q. Ye, L. Xiang, X. Qiu, S. Liu, Z. Deng, J. Zhou, S. Liu, S. Shi, Y. Jin, Apoptotic vesicles restore liver macrophage homeostasis to counteract type 2 diabetes, J. Extracell. Vesicles 10 (7) (2021).
[21] X. Kou, X. Xu, C. Chen, M.L. Sanmillan, T. Cai, Y. Zhou, C. Giraudo, A. Le, S. Shi, The Fas/Fap-1/Cav-1 complex regulates IL-1RA secretion in mesenchymal stem cells to accelerate wound healing, Sci. Transl. Med. 10 (432) (2018).
[22] E.N. Marieb, K. Hoehn, Human Anatomy & Physiology, seventh ed., Pearson Benjamin Cummings, San Francisco, 2007.
[23] C.J. Weschler, S. Langer, A. Fischer, G. Bekö, J. Toftum, G. Clausen, Squalene and cholesterol in dust from Danish homes and daycare centers, Environ. Sci. Technol. 45 (9) (2011) 3872–3879.
[24] A.S. Cheng, S.J. Bayliss, The genetics of hair shaft disorders, J. Am. Acad. Dermatol. 59 (1) (2008) 1–22, quiz 23-6.
[25] P.K. Wallace, J.D. Tario Jr., J.L. Fisher, S.S. Wallace, M.S. Ernstoff, K.A. Muirhead, Tracking antigen-driven responses by flow cytometry: monitoring proliferation by dye dilution, Cytometry 73 (11) (2008) 1019–1034.
[26] Z. Zheng, H.X. Liu, S.D. Zhai, H.K. Zhang, G.G. Shan, R.T.K. Kwok, C. Ma, H.H. Y. Sung, I.D. Williams, J.W.Y. Lam, K.S. Wong, X.L. Hu, B. Tang, Highly efficient singlet oxygen generation, two-photon photodynamic therapy and melanoma ablation by rationally designed mitochondria-specific near-infrared AIEgens, Chem. Sci. 11 (9) (2020) 2494–2503.
[27] Z. Zheng, T. Zhang, H. Liu, Y. Chen, R.T.K. Kwok, C. Ma, P. Zhang, H.H.Y. Sung, I. D. Williams, J.W.Y. Lam, K.S. Wong, B.Z. Tang, Bright near-infrared aggregation-induced emission luminogens with strong two-photon absorption, excellent organelle specificity, and efficient photodynamic therapy potential, ACS Nano 12 (8) (2018) 8145–8159.
[28] T. Tumbar, G. Guasch, V. Greco, C. Blanpain, W.E. Lowry, M. Rendl, E. Fuchs, Defining the epithelial stem cell niche in skin, Science 303 (5656) (2004) 359–363.
[29] L. Katsimpardi, N.K. Litterman, P.A. Schein, C.M. Miller, F.S. Loffredo, G. R. Wojtkiewicz, J.W. Chen, R.T. Lee, A.J. Wagers, L.L. Rubin, Vascular and neurogenic rejuvenation of the aging mouse brain by young systemic factors, Science 344 (6184) (2014) 630–634.
[30] J.L. Li, C.C. Goh, J.L. Keeble, J.S. Qin, B. Roediger, R. Jain, Y. Wang, W.K. Chew, W. Weninger, L.G. Ng, Intravital multiphoton imaging of immune responses in the mouse ear skin, Nat. Protoc. 7 (2) (2012) 221–234.
[31] K.R. Mesa, P. Rompolas, G. Zito, P. Myung, T.Y. Sun, S. Brown, D.G. Gonzalez, K. B. Blagoev, A.M. Haberman, V. Greco, Niche-induced cell death and epithelial phagocytosis regulate hair follicle stem cell pool, Nature 522 (7554) (2015) 94–97.
[32] Y.S. Choi, Y. Zhang, M. Xu, Y. Yang, M. Ito, T. Peng, Z. Cui, A. Nagy, A.-K. Hadjantonakis, R.A. Lang, G. Cotsarelis, T. Andl, E.E. Morrisey, S.E. Millar, Distinct functions for Wnt/β-catenin in hair follicle stem cell proliferation and survival and interfollicular epidermal homeostasis, Cell Stem Cell 13 (6) (2013) 720–733.
[33] A. Veltri, C. Lang, W.H. Lien, Concise review: Wnt signaling pathways in skin development and epidermal stem cells, Stem Cell. 36 (1) (2018) 22–35.
[34] P. Clément-Lacroix, M. Ai, F. Morvan, S. Roman-Roman, B. Vayssière, C. Belleville, K. Estrera, M.L. Warman, R. Baron, G. Rawadi, Lrp5-independent activation of Wnt signaling by lithium chloride increases bone formation and bone mass in mice, Proc. Natl. Acad. Sci. U. S. A. 102 (48) (2005) 17406–17411.
[35] S.M. Huang, Y.M. Mishina, S. Liu, A. Cheung, F. Stegmeier, G.A. Michaud, O. Charlat, E. Wiellette, Y. Zhang, S. Wiessner, M. Hild, X. Shi, C.J. Wilson, C. Mickanin, V. Myer, A. Fazal, R. Tomlinson, F. Serluca, W. Shao, H. Cheng,

M. Shultz, C. Rau, M. Schirle, J. Schlegl, S. Ghidelli, S. Fawell, C. Lu, D. Curtis, M. W. Kirschner, C. Lengauer, P.M. Finan, J.A. Tallarico, T. Bouwmeester, J.A. Porter, A. Bauer, F. Cong, Tankyrase inhibition stabilizes axin and antagonizes Wnt signalling, Nature 461 (7264) (2009) 614–620.
[36] D. Pinheiro, Y. Bellaïche, Mechanical force-driven adherens junction remodeling and epithelial dynamics, Dev. Cell 47 (1) (2018) 3–19.
[37] M. Huse, Mechanical forces in the immune system, Nat. Rev. Immunol. 17 (11) (2017) 679–690.
[38] J.M. Barnes, L. Przybyla, V.M. Weaver, Tissue mechanics regulate brain development, homeostasis and disease, J. Cell Sci. 130 (1) (2017) 71–82.
[39] L. Przybyla, J.M. Muncie, V.M. Weaver, Mechanical control of epithelial-to-mesenchymal transitions in development and cancer, Annu. Rev. Cell Dev. Biol. 32 (2016) 527–554.
[40] B. Cha, X. Geng, M.R. Mahamud, J. Fu, A. Mukherjee, Y. Kim, E.H. Jho, T.H. Kim, M.L. Kahn, L. Xia, J.B. Dixon, H. Chen, R.S. Srinivasan, Mechanotransduction activates canonical Wnt/β-catenin signaling to promote lymphatic vascular patterning and the development of lymphatic and lymphovenous valves, Genes Dev. 30 (12) (2016) 1454–1469.
[41] J.R. Hens, K.M. Wilson, P. Dann, X. Chen, M.C. Horowitz, J.J. Wysolmerski, TOPGAL mice show that the canonical Wnt signaling pathway is active during bone development and growth and is activated by mechanical loading in vitro, J. Bone Miner. Res. 20 (7) (2005) 1103–1113.
[42] J. Drappa, N. Brot, K.B. Elkon, The Fas protein is expressed at high levels on CD4+ CD8+ thymocytes and activated mature lymphocytes in normal mice but not in the lupus-prone strain, MRL lpr/lpr, Proc. Natl. Acad. Sci. U. S. A. 90 (21) (1993) 10340–10344.
[43] C.E. Fogarty, A. Bergmann, Killers creating new life: caspases drive apoptosis-induced proliferation in tissue repair and disease, Cell Death Differ. 24 (8) (2017) 1390–1400.
[44] F. Li, Q. Huang, J. Chen, Y. Peng, D.R. Roop, J.S. Bedford, C.Y. Li, Apoptotic cells activate the "phoenix rising" pathway to promote wound healing and tissue regeneration, Sci. Signal. 3 (110) (2010) ra13.
[45] J.L. Whyte, A.A. Smith, J.A. Helms, Wnt signaling and injury repair, Cold Spring Harbor Perspect. Biol. 4 (8) (2012), a008078.
[46] S. Müller-Röver, B. Handjiski, C. van der Veen, S. Eichmüller, K. Foitzik, I. A. McKay, K.S. Stenn, R. Paus, A comprehensive guide for the accurate classification of murine hair follicles in distinct hair cycle stages, J. Invest. Dermatol. 117 (1) (2001) 3–15.
[47] N. Sato, P.L. Leopold, R.G. Crystal, Induction of the hair growth phase in postnatal mice by localized transient expression of Sonic hedgehog, J. Clin. Invest. 104 (7) (1999) 855–864.
[48] J. Huelsken, R. Vogel, B. Erdmann, G. Cotsarelis, W. Birchmeier, beta-Catenin controls hair follicle morphogenesis and stem cell differentiation in the skin, Cell 105 (4) (2001) 533–545.
[49] D. Van Mater, F.T. Kolligs, A.A. Dlugosz, E.R. Fearon, Transient activation of beta -catenin signaling in cutaneous keratinocytes is sufficient to trigger the active growth phase of the hair cycle in mice, Genes Dev. 17 (10) (2003) 1219–1224.
[50] B.A. Morgan, The dermal papilla: an instructive niche for epithelial stem and progenitor cells in development and regeneration of the hair follicle, Cold Spring Harb. Perspect. Med. 4 (7) (2014), a015180.
[51] S. Morioka, C. Maueröder, K.S. Ravichandran, Living on the edge: efferocytosis at the interface of homeostasis and pathology, Immunity 50 (5) (2019) 1149–1162.
[52] T. Squillaro, G. Peluso, U. Galderisi, Clinical trials with mesenchymal stem cells: an update, Cell Transplant. 25 (5) (2016) 829–848.
[53] R.H. Lee, A.A. Pulin, M.J. Seo, D.J. Kota, J. Ylostalo, B.L. Larson, L. Semprun-Prieto, P. Delafontaine, D.J. Prockop, Intravenous hMSCs improve myocardial infarction in mice because cells embolized in lung are activated to secrete the anti-inflammatory protein TSG-6, Cell Stem Cell 5 (1) (2009) 54–63.
[54] K. Akiyama, C. Chen, D. Wang, X. Xu, C. Qu, T. Yamaza, T. Cai, W. Chen, L. Sun, S. Shi, Mesenchymal-stem-cell-induced immunoregulation involves FAS-ligand-/FAS-mediated T cell apoptosis, Cell Stem Cell 10 (5) (2012) 544–555.
[55] A. Galleu, Y. Riffo-Vasquez, C. Trento, C. Lomas, L. Dolcetti, T.S. Cheung, M. von Bonin, L. Barbieri, K. Halai, S. Ward, L. Weng, R. Chakraverty, G. Lombardi, F. M. Watt, K. Orchard, D.I. Marks, J. Apperley, M. Bornhauser, H. Walczak, C. Bennett, F. Dazzi, Apoptosis in mesenchymal stromal cells induces in vivo recipient-mediated immunomodulation, Sci. Transl. Med. 9 (416) (2017).
[56] B. Crivelli, T. Chlapanidas, S. Perteghella, E. Lucarelli, L. Pascucci, A.T. Brini, I. Ferrero, M. Marazzi, A. Pessina, M.L. Torre, Mesenchymal stem/stromal cell extracellular vesicles: from active principle to next generation drug delivery system, J. Contr. Release 262 (2017) 104–117.
[57] W.S. Park, S.Y. Ahn, S.I. Sung, J.Y. Ahn, Y.S. Chang, Strategies to enhance paracrine potency of transplanted mesenchymal stem cells in intractable neonatal disorders, Pediatr. Res. 83 (1–2) (2018) 214–222.
[58] I.M. Conboy, M.J. Conboy, A.J. Wagers, E.R. Girma, I.L. Weissman, T.A. Rando, Rejuvenation of aged progenitor cells by exposure to a young systemic environment, Nature 433 (7027) (2005) 760–764.
[59] A. Bitto, M. Kaeberlein, Rejuvenation: it's in our blood, Cell Metabol. 20 (1) (2014) 2–4.
[60] D. Enshell-Seijffers, C. Lindon, M. Kashiwagi, B.A. Morgan, beta-catenin activity in the dermal papilla regulates morphogenesis and regeneration of hair, Dev. Cell 18 (4) (2010) 633–642.
[61] P.S. Myung, M. Takeo, M. Ito, R.P. Atit, Epithelial Wnt ligand secretion is required for adult hair follicle growth and regeneration, J. Invest. Dermatol. 133 (1) (2013) 31–41.
[62] D.A. Winter, Moments of force and mechanical power in jogging, J. Biomech. 16 (1) (1983) 91–97.
[63] N. Yamazaki, K. Ohta, Y. Ohgi, Mechanical energy transfer by internal force during the swing phase of running, Procedia Eng. 34 (2012) 772–777.
[64] J. Wang, C.D. Wang, N. Zhang, W.X. Tong, Y.F. Zhang, S.Z. Shan, X.L. Zhang, Q. F. Li, Mechanical stimulation orchestrates the osteogenic differentiation of human bone marrow stromal cells by regulating HDAC1, Cell Death Dis. 7 (5) (2016) e2221-e2221.
[65] W. Yu, C. Chen, X. Kou, B. Sui, T. Yu, D. Liu, R. Wang, J. Wang, S. Shi, Mechanical force-driven TNFα endocytosis governs stem cell homeostasis, Bone Res. 8 (1) (2021) 44.
[66] T.H. Kim, J.S. Chang, K.S. Park, J. Park, N. Kim, J.I. Lee, I.D. Kong, Effects of exercise training on circulating levels of Dickkpof-1 and secreted frizzled-related protein-1 in breast cancer survivors: a pilot single-blind randomized controlled trial, PLoS One 12 (2) (2017), e0171771.
[67] P. Klentrou, K. Angrish, N. Awadia, N. Kurgan, R. Kouvelioti, B. Falk, Wnt signaling-related osteokines at rest and following plyometric exercise in prepubertal and early pubertal boys and girls, Pediatr. Exerc. Sci. 30 (4) (2018) 457–465.
[68] J. Dekker, K. Nelson, N. Kurgan, B. Falk, A. Josse, P. Klentrou, Wnt signaling-related osteokines and transforming growth factors before and after a single bout of plyometric exercise in child and adolescent females, Pediatr. Exerc. Sci. 29 (4) (2017) 504–512.
[69] K. Kerschan-Schindl, M.M. Thalmann, E. Weiss, M. Tsironi, U. Föger-Samwald, J. Meinhart, K. Skenderi, P. Pietschmann, Changes in serum levels of myokines and wnt-antagonists after an ultramarathon race, PLoS One 10 (7) (2015), e0132478.
[70] A.G. Robling, P.J. Niziolek, L.A. Baldridge, K.W. Condon, M.R. Allen, I. Alam, S. M. Mantila, J. Gluhak-Heinrich, T.M. Bellido, S.E. Harris, C.H. Turner, Mechanical stimulation of bone in vivo reduces osteocyte expression of Sost/sclerostin, J. Biol. Chem. 283 (9) (2008) 5866–5875.
[71] S. Nagata, Apoptosis and autoimmune diseases, Ann. N. Y. Acad. Sci. 1209 (2010) 10–16.
[72] J. Cheng, T. Zhou, C. Liu, J.P. Shapiro, M.J. Brauer, M.C. Kiefer, P.J. Barr, J. D. Mountz, Protection from Fas-mediated apoptosis by a soluble form of the Fas molecule, Science 263 (5154) (1994) 1759–1762.
[73] F. Furukawa, H. Tanaka, K. Sekita, T. Nakamura, Y. Horiguchi, Y. Hamashima, Dermatopathological studies on skin lesions of MRL mice, Arch. Dermatol. Res. 276 (3) (1984) 186–194.
[74] A.E. Russell, A. Sneider, K.W. Witwer, P. Bergese, S.N. Bhattacharyya, A. Cocks, E. Cocucci, U. Erdbrügger, J.M. Falcon-Perez, D.W. Freeman, T.M. Gallagher, S. Hu, Y. Huang, S.M. Jay, S.I. Kano, G. Lavieu, A. Leszczynska, A.M. Llorente, Q. Lu, V. Mahairaki, D.C. Muth, N. Noren Hooten, M. Ostrowski, I. Prada, S. Sahoo, T.H. Schøyen, L. Sheng, D. Tesch, G. Van Niel, R.E. Vandenbroucke, F.J. Verweij, A. V. Villar, M. Wauben, A.M. Wehman, H. Yin, D.R.F. Carter, P. Vader, Biological membranes in EV biogenesis, stability, uptake, and cargo transfer: an ISEV position paper arising from the ISEV membranes and EVs workshop, J. Extracell. Vesicles 8 (1) (2019), 1684862.
[75] L. Mashouri, H. Yousefi, A.R. Aref, A.M. Ahadi, F. Molaei, S.K. Alahari, Exosomes: composition, biogenesis, and mechanisms in cancer metastasis and drug resistance, Mol. Cancer 18 (1) (2019) 75.
[76] H. Kalra, G.P.C. Drummen, S. Mathivanan, Focus on extracellular vesicles: introducing the next small big thing, Int. J. Mol. Sci. 17 (2) (2016), 170-170.
[77] F.G. Kugeratski, K. Hodge, S. Lilla, K.M. McAndrews, X. Zhou, R.F. Hwang, S. Zanivan, R. Kalluri, Quantitative proteomics identifies the core proteome of exosomes with syntenin-1 as the highest abundant protein and a putative universal biomarker, Nat. Cell Biol. 23 (6) (2021) 631–641.
[78] T.J. Shaw, P. Martin, Wound repair at a glance, J. Cell Sci. 122 (Pt 18) (2009) 3209–3213.
[79] K.S. Houschyar, A. Momeni, M.N. Pyles, Z.N. Maan, A.J. Whittam, F. Siemers, Wnt signaling induces epithelial differentiation during cutaneous wound healing, Organogenesis 11 (3) (2015) 95–104.
[80] M. Riazifar, E.J. Pone, J. Lötvall, W. Zhao, Stem cell extracellular vesicles: extended messages of regeneration, Annu. Rev. Pharmacol. Toxicol. 57 (2017) 125–154.
[81] J. Cabral, A.E. Ryan, M.D. Griffin, T. Ritter, Extracellular vesicles as modulators of wound healing, Adv. Drug Deliv. Rev. 129 (2018) 394–406.
[82] B. Zhang, M. Wang, A. Gong, X. Zhang, X. Wu, Y. Zhu, H. Shi, L. Wu, W. Zhu, H. Qian, W. Xu, HucMSC-exosome mediated-wnt4 signaling is required for cutaneous wound healing, Stem Cell. 33 (7) (2015) 2158–2168.
[83] S. Werner, T. Krieg, H. Smola, Keratinocyte-fibroblast interactions in wound healing, J. Invest. Dermatol. 127 (5) (2007) 998–1008.
[84] K. Sivamani Raja, M.S. Garcia, R.R. Isseroff, Wound re-epithelialization: modulating keratinocyte migration in wound healing, Front. Biosci. 12 (2007) 2849–2868.
[85] L. Alonso, E. Fuchs, The hair cycle, J. Cell Sci. 119 (Pt 3) (2006) 391–393.
[86] J. Kishimoto, R.E. Burgeson, B.A. Morgan, Wnt signaling maintains the hair-inducing activity of the dermal papilla, Genes Dev. 14 (10) (2000) 1181–1185.
[87] D. Chen, A. Jarrell, C. Guo, R. Lang, R. Atit, Dermal β-catenin activity in response to epidermal Wnt ligands is required for fibroblast proliferation and hair follicle initiation, Development 139 (8) (2012) 1522–1533.
[88] L. Horev, Environmental and cosmetic factors in hair loss and destruction, Curr. Probl. Dermatol. 35 (2007) 103–117.
[89] S.P. Hagenaars, W.D. Hill, S.E. Harris, S.J. Ritchie, G. Davies, D.C. Liewald, C. R. Gale, D.J. Porteous, I.J. Deary, R.E. Marioni, Genetic prediction of male pattern baldness, PLoS Genet. 13 (2) (2017), e1006594.
[90] A. Rossi, C. Cantisani, L. Melis, A. Iorio, E. Scali, S. Calvieri, Minoxidil use in dermatology, side effects and recent patents, Recent Pat. Inflamm. Allergy Drug Discov. 6 (2) (2012) 130–136.

[91] P. Gentile, S. Garcovich, Advances in regenerative stem cell therapy in androgenic alopecia and hair loss: Wnt pathway, growth-factor, and mesenchymal stem cell signaling impact analysis on cell growth and hair follicle development, Cells 8 (5) (2019) 466.
[92] D.H. Bak, M.J. Choi, S.R. Kim, B.C. Lee, J.M. Kim, E.S. Jeon, W. Oh, E.S. Lim, B. C. Park, M.J. Kim, J. Na, B.J. Kim, Human umbilical cord blood mesenchymal stem cells engineered to overexpress growth factors accelerate outcomes in hair growth, KOREAN J. PHYSIOL. PHARMACOL. 22 (5) (2018) 555–566.
[93] R.L. Rajendran, P. Gangadaran, S.S. Bak, J.M. Oh, S. Kalimuthu, H.W. Lee, S. H. Baek, L. Zhu, Y.K. Sung, S.Y. Jeong, S.W. Lee, J. Lee, B.C. Ahn, Extracellular vesicles derived from MSCs activates dermal papilla cell in vitro and promotes hair follicle conversion from telogen to anagen in mice, Sci. Rep. 7 (1) (2017), 15560.
[94] R.L. Rajendran, P. Gangadaran, C.H. Seo, M.H. Kwack, J.M. Oh, H.W. Lee, A. Gopal, Y.K. Sung, S.Y. Jeong, S.W. Lee, J. Lee, B.C. Ahn, Macrophage-derived extracellular vesicle promotes hair growth, Cells 9 (4) (2020).
[95] A. le Riche, E. Aberdam, L. Marchand, E. Frank, C. Jahoda, I. Petit, S. Bordes, B. Closs, D. Aberdam, Extracellular vesicles from activated dermal fibroblasts stimulate hair follicle growth through dermal papilla-secreted norrin, Stem Cell. 37 (9) (2019) 1166–1175.
[96] Y. Tian, L. Ma, M. Gong, G. Su, S. Zhu, W. Zhang, S. Wang, Z. Li, C. Chen, L. Li, L. Wu, X. Yan, Protein profiling and sizing of extracellular vesicles from colorectal cancer patients via flow cytometry, ACS Nano 12 (1) (2018) 671–680.
[97] K. Gledhill, A. Gardner, C.A. Jahoda, Isolation and establishment of hair follicle dermal papilla cell cultures, Methods Mol. Biol. 989 (2013) 285–292.
[98] C.A. Jahoda, J. Whitehouse, A.J. Reynolds, N. Hole, Hair follicle dermal cells differentiate into adipogenic and osteogenic lineages, Exp. Dermatol. 12 (6) (2003) 849–859.
[99] P. Rompolas, E.R. Deschene, G. Zito, D.G. Gonzalez, I. Saotome, A.M. Haberman, V. Greco, Live imaging of stem cell and progeny behaviour in physiological hair-follicle regeneration, Nature 487 (7408) (2012) 496–499.